nature communications

Article

https://doi.org/10.1038/s41467-025-62134-w

Mogat1 drives metabolic adaptations to evade immune surveillance

Received: 1 August 2024

Accepted: 11 July 2025

Published online: 31 July 2025

Check for updates

Huan Wei[1,2,8], Congyi Niu[1,8], Yue Shi[3,4,8], Yingfei Fang[2], Chengheng Yang[2,5], Jian Liu[6] & Zhenjie Xu[2,3,4,5,7]

Immune checkpoint blockade (ICB) therapies for solid tumors often fail due to resistance, necessitating new strategies. While efforts target IFNγ signaling or antigen presentation, other immune evasion mechanisms are unclear. Here, we identify Monoacylglycerol O-Acyltransferase 1 (Mogat1) as a critical modulator of tumor immune evasion using an in vivo transcriptomic screen in progressing tumors. We find that tumors exploit Mogat1 to sequester fatty acids into triglycerides, a metabolic adaptation that fuels growth and fosters an immunosuppressive microenvironment, enabling immune escape. Genetic inhibition of Mogat1 suppresses tumor growth by promoting T-cell infiltration and enhancing their tumor-killing ability. Importantly, Mogat1 loss sensitizes tumors to PD-1 blockade, overcoming resistance and suggesting reduced reliance on conventional antigen presentation. Our findings reveal a lipid metabolism-centered immune evasion mechanism and highlight Mogat1 as a potential target to improve cancer immunotherapy.

Immune checkpoint blockade (ICB) therapies have achieved remarkable clinical success, yet a majority of patients either fail to respond initially or develop acquired resistance[1–5]. This resistance is often attributed to tumor-intrinsic alterations, such as mutations disrupting interferon-γ (IFNγ) signaling or antigen presentation pathways[1–5]. Critically, effective strategies to overcome acquired ICB resistance are lacking, underscoring the urgent need for alternative approaches that can reignite anti-tumor immunity within the tumor microenvironment (TME).

While genome-wide genetic perturbation screens (e.g., CRISPR-Cas9) provide valuable insights into gene function[4–7], particularly in vitro or under simplified in vivo conditions, they may not fully capture the adaptive changes occurring during tumor progression within a complex, evolving TME. Such screens identify effects following introduced modifications. Recognizing these limitations, we pursued a distinct approach: an in vivo selection strategy using longitudinal transcriptomic analysis to identify genes whose expression is naturally modulated by immune pressure during tumor development.

To decipher the dynamic interplay between tumor cells and the immune system during cancer progression, we first characterized the evolving immune landscape in an immunocompetent mouse model of MMTV-PyMT breast cancer. Building on this model, we employed an unbiased in vivo selection strategy coupled with transcriptomic profiling across different stages of tumor development. This approach, designed to capture genes naturally enriched under immune pressure, led us to identify a previously uncharacterized role for Monoacylglycerol O-acyltransferase 1 (Mogat1) in tumor immune evasion. Mogat1 is a key enzyme in triglyceride (TAG) synthesis, catalyzing the formation of diacylglycerol (DAG) from monoacylglycerol (MAG)[8]. Its expression is typically restricted to metabolically active tissues like the intestine, liver, and adipose tissue[9,10], where it influences systemic metabolism; for instance, hepatic Mogat1 inhibition improves glucose homeostasis[11]. Despite its known roles in normal physiology and hepatic steatosis, the function of Mogat1 in cancer biology, particularly within the TME, has remained unexplored. Here, we reveal an unexpected role for Mogat1 in driving metabolic adaptations during tumor

[1]School of Basic Medical Science, Fudan University, Shanghai, China. [2]School of Life Sciences, Westlake University, Hangzhou, Zhejiang, China. [3]School of Life Sciences, Fudan University, Shanghai, China. [4]Westlake University Research Center for Industries of the Future, Westlake University, Hangzhou, Zhejiang, China. [5]Westlake Laboratory of Life Sciences and Biomedicine, Hangzhou, Zhejiang, China. [6]Department of Breast Surgery, Affiliated Hangzhou First People's Hospital, School of Medicine, Westlake University, Hangzhou, Zhejiang, China. [7]School of Medicine, Zhejiang University, Hangzhou, Zhejiang, China. [8]These authors contributed equally: Huan Wei, Congyi Niu, Yue Shi. e-mail: xuzhenjie@westlake.edu.cn

progression. We demonstrate that tumor cells leverage Mogat1 to sequester excess fatty acids into TAG stored in lipid droplets, effectively rewiring metabolic pathways to simultaneously fuel growth and establish an immunosuppressive niche. This study unveils a lipid metabolism-centric mechanism of immune evasion mediated by Mogat1 and identifies it as a promising therapeutic target to enhance cancer immunotherapy.

Results

Immune infiltration dynamics during breast cancer progression

A robust anti-tumor immune response is critical in suppressing tumor development. However, tumor cells often evolve mechanisms to evade immune surveillance, enabling their survival and expansion. Uncovering the genetic drivers of this immune escape is essential for developing effective immunotherapies.

As an alternative to direct genetic manipulation approaches, we employed an unbiased in vivo selection strategy coupled with transcriptomic profiling to identify genes whose expression is naturally modulated during tumor progression under immune pressure. By analyzing the transcriptomes of tumor cells isolated at various stages of development within an immunocompetent host, we aimed to capture dynamic gene expression changes reflecting the intricate tumor-immune interactions across different phases of progression. We reasoned that leveraging the natural selective pressures of the host immune system in situ would allow us to identify clinically relevant adaptive changes potentially missed by in vitro or simplified in vivo perturbation screens. Specifically, instead of introducing exogenous genetic modifications, we injected GFP-expressing MMTV-PyMT breast cancer cells into the mammary fat pads of immunocompetent FVB mice, allowing the tumors to evolve naturally. We hypothesized that subsequent transcriptomic analysis of tumor cells harvested at distinct time points would reveal genes upregulated or downregulated through natural selection, thereby identifying factors essential for tumor growth and immune evasion in this physiologically relevant context.

Following tumor induction, we monitored tumor growth and conducted detailed immune profiling weekly (Fig. 1a). This approach allowed us to track the kinetics of immune cell responses within the tumor microenvironment as tumors progressed from early to late stages (Fig. 1b). As expected, flow cytometry analysis revealed a significant decline in both the number and percentage of tumor-infiltrating $CD45^+$ immune cells as tumors advanced (Fig. 1c, e), a finding confirmed by immunofluorescence analysis of $CD45^+$ cells in tumor sections (Fig. 1f, h). This progressive decline in immune cell infiltration led to a global reshaping of the tumor immune compartment. We further validated this observation using the MMTV-PyMT spontaneous breast cancer genetically engineered mouse model (GEMM), which also demonstrated a progressive decrease in $CD45^+$ immune cell infiltration with tumor progression (Supplementary Fig. 1a, b and Supplementary Fig. 1e, f). This convergence of findings across both models confirms that our transplantation model effectively mirrors key aspects of immune modulation observed during spontaneous tumor development.

To further dissect the evolving immune landscape within TME, we characterized the dynamic changes in immune cell subsets. We observed a marked shift in the balance between lymphoid and myeloid lineages within the $CD45^+$ compartment (Supplementary Fig. 2a, b). Specifically, the proportion of lymphoid cells decreased significantly, while myeloid cells became progressively enriched as tumors expanded (Supplementary Fig. 2a, b). Within the TME, infiltrating myeloid-derived suppressor cells (MDSCs) and tumor-associated macrophages (TAMs) play important regulatory roles in immunosuppression of tumor hosts to promote tumor progression and modulate the function of tumor-infiltrating lymphocytes[12,13]. Among myeloid cells, MDSCs exhibited the most dramatic increase over time (Supplementary Fig. 2c, d), consistent with their established role in creating a pro-tumorigenic immunosuppressive environment[14,15], while TAMs proportions remained relatively stable (Supplementary Fig. 2c, d), as previously reported in established tumors[16].

While the percentage of total T cells progressively declined within the lymphoid compartment (Fig. 1i, j), the composition of the T cell compartment shifted. Although $CD8^+$ T cells as a percentage of total T cells showed a moderate increase, peaking in the middle and late stages of tumor growth (Supplementary Fig. 2e, f), the overall decline in total T cells suggests this did not represent a substantial increase in absolute $CD8^+$ T cell numbers. In contrast, the proportion of $CD4^+$ T cells steadily decreased throughout tumor progression (Supplementary Fig. 2e, f). Concurrently, we observed a marked expansion of both NK cell populations, increasing by ~5-fold during tumor development (Fig. 1i, Supplementary Fig. 2g). These immune shifts mirrored findings in the MMTV-PyMT GEMM model, where the proportion of $CD3^+$ T cells within $CD45^+$ immune cells progressively declined (Supplementary Fig. 1c, d), and $CD8^+$ T cell infiltration into tumor tissue diminished (Supplementary Fig. 1e, g). Similarly, NK cell proportions gradually increased with tumor progression in the MMTV-PyMT model (Supplementary Fig. 2g), further underscoring the conserved nature of these immune dynamics. Collectively, these results demonstrate that the progressive decline in immune infiltration and the resulting remodeling of the tumor immune compartment recapitulate key features of immune responses observed in spontaneous breast cancer model.

Importantly, RNA sequencing of intratumoral $CD8^+$ T cells isolated at different stages of tumor progression revealed a progressive upregulation of inhibitory receptors including Pd1, Lag3, and Tigit (Supplementary Fig. 2h), consistent with previously described patterns of T cell exhaustion[17–19]. Notably, this upregulation of immune checkpoint molecules occurred simultaneously with increased expression of cytotoxic effector molecules like Granzyme B, IFNγ, and TNF-α, reflecting the complex dynamics of T cell responses within the tumor microenvironment[19,20]. This pattern suggests a state of T cell exhaustion that develops progressively during tumor growth[20,21], characterized by the paradoxical co-expression of both inhibitory and effector programs[22]. Together, these results highlight the dynamic and evolving nature of the tumor immune microenvironment during breast cancer progression[23]. While our MMTV-PyMT transplantation model differs experimentally from spontaneous tumor development, this detailed characterization confirms that it effectively recapitulates key immunological features, including evolving immune-tumor cell interactions and the establishment of an immunosuppressive environment characteristic of breast cancer progression[24,25], thus validating its suitability for our subsequent investigations into the molecular drivers of these processes.

Mogat1 expression increases along breast tumor advancement and correlates with lipid accumulation

Tumor expansion necessitates acquiring immune evasion mechanisms that enable cancer cells to circumvent immune surveillance. To unveil the molecular underpinnings of tumor immune evasion and growth using the strategy outlined above, we performed RNA sequencing on GFP-expressing MMTV-PyMT tumor cells isolated at early (week 1–2), middle (week 3), and late (week 4) stages of tumor development in our model (Fig. 1a). Principal component analysis (PCA) and clustering analysis revealed distinct transcriptional profiles for each stage, highlighting the dynamic evolution of tumor cells during progression (Fig. 2a).

Intriguingly, our analysis identified 34 genes that were consistently upregulated throughout tumor development from early to late stages (Fig. 2b, c). Among these 34 genes, Mogat1, encoding monoacylglycerol O-acyltransferase 1, a key enzyme in triglyceride synthesis[8], emerged as the prominently upregulated gene in late-stage

https://doi.org/10.1038/s41467-025-62134-w

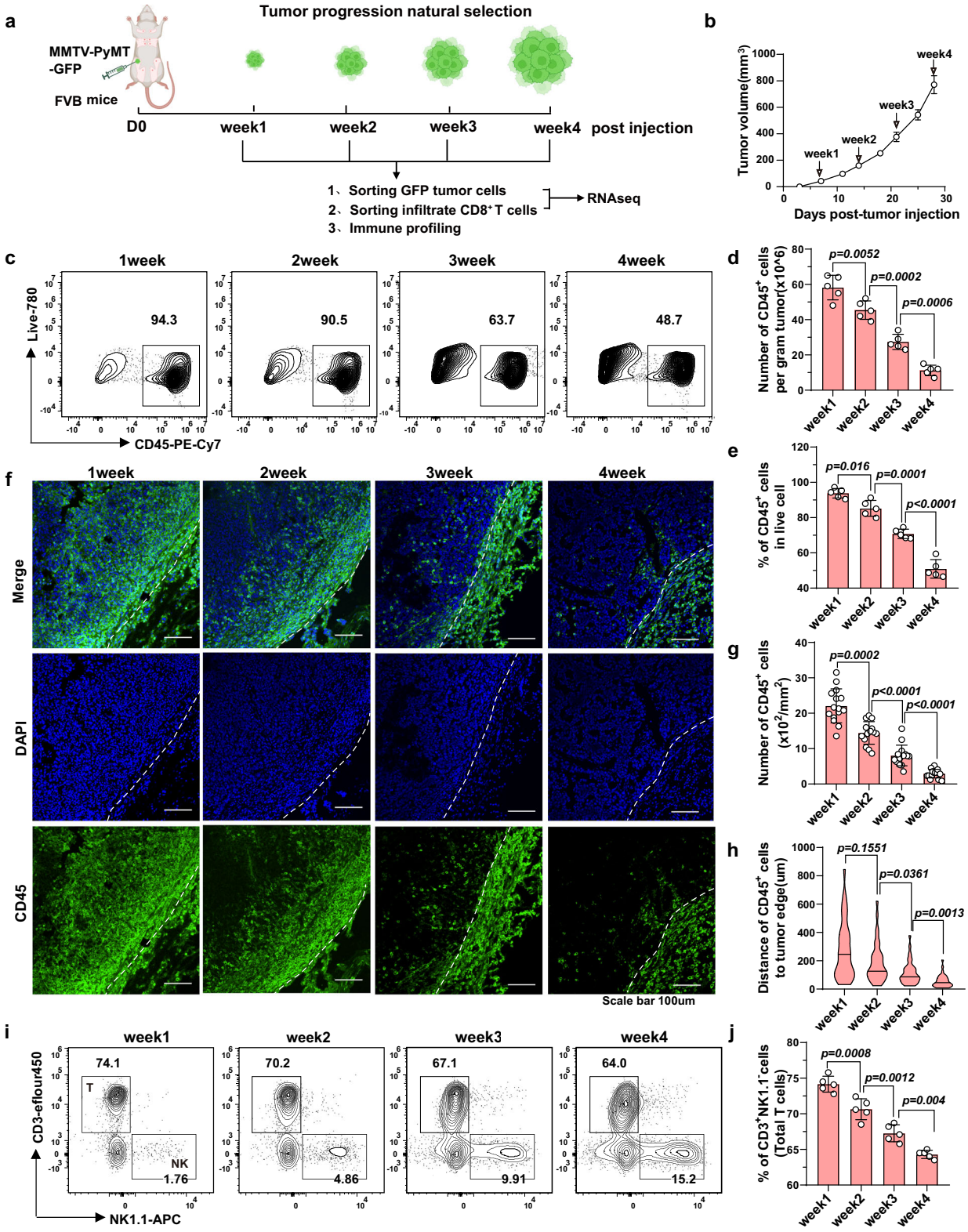

tumors (Fig. 2c, d and Supplementary Fig. 3a).Differential gene expression analysis revealed a significant upregulation of genes associated with energy metabolism, particularly lipid metabolism, as tumors progressed. Compared to early-stage tumors, middle-stage tumors exhibited significant enrichment of pathways related to negative regulation of lipid transport, PI3K signaling, and cellular metabolic processes (Supplementary Fig. 3b). This metabolic shift persisted in late-stage tumors, which showed further enrichment of lipid and fatty acid metabolism pathways (Fig. 2e). Collectively, these transcriptomic shifts suggest that adaptations in lipid metabolism, potentially involving Mogat1, may play an important role during tumor development.

We sought to define Mogat1's unique role by comparing its expression with other triglyceride synthesis genes in the monoacylglycerol (*Mogat2, Dgat1, Dgat2*; 26) and glycerol-3-phosphate (*Gpat, Agpat1-5*; 27) pathways (Supplementary Fig. 3c, d). Notably, while most other lipid metabolism synthases, including Agpat3-5,

Fig. 1 | Immune infiltration dynamics during breast cancer progression. **a** Schematic diagram of the orthotopic breast cancer model utilizing MMTV-PyMT tumor cells inoculated into fat pad of immunocompetent FVB mice. Created in BioRender. https://BioRender.com/penf9v4. **b** Tumor growth kinetics of MMTV-PyMT tumors in FVB mice (n = 5 mice per group). **c**–**e** Flow cytometry analysis of total immune cell infiltration in MMTV-PyMT tumors at different time points. **c** Percentage of $CD45^+$ immune cells among live cells within the tumor. **d** Total number of $CD45^+$ immune cells isolated from per gram tumors. **e** Representative flow cytometry plots $CD45^+$ immune cells gated on live cells. (n = 5 mice per group). **f** Representative immunofluorescence images of MMTV-PyMT tumor sections at indicated time points, stained for CD45 (green) to visualize total immune cells. Scale bar: 100 µm. **g** Quantification of $CD45^+$ immune cell density (cells/mm^2) in MMTV-PyMT tumors. (Data represent the mean value from n = 5 biologically independent mice per group. For each mouse, 3 tumor sections were analyzed, and the average value was used for plotting and statistical analysis.). **h** Quantification of the distance between $CD45^+$ cells and the tumor margin in MMTV-PyMT tumors, assessed from immunofluorescence images. (Data represent the mean value from n = 5 biologically independent mice per group.). **i**, **j** Flow cytometry analysis of T cell and NK cells within the tumor-infiltrating lymphocyte population at different time points. **i** Representative flow cytometry plots gated on lymphoid cells (gated $CD45^+$ $CD11B^-$ cells). **j** Quantification of T cells ($CD3^+$ $NK1.1^-$) as a percentage of lymphoid cells. The gating strategy for these panels is further detailed in Supplementary Fig 2a. (n = 5 mice per group). Data **c**–**j** are representative of two independent experiments from 5 mice per group per experiment. Data are presented as mean ± SD (**d**, **e**, **g**, **h**, **j**) and mean ± SEM (**b**). Statistical significance was calculated using one-way ANOVA (**d**, **e**, **g**, **h**, **j**). Source data are provided as a Source Data file.

exhibited unchanged or decreased expression, Mogat1 was consistently upregulated throughout tumor progression (Fig. 2f and Supplementary Fig. 3c, d), an observation corroborated by qPCR (Fig. 2g). In the MMTV-PyMT GEMM model, we observed higher mogat1 expression in tumor tissues compared to normal mammary glands, with expression further increasing during tumor progression (Fig. 2h), while its levels remained stable in normal mammary glands across different ages (Supplementary Fig. 3e). This pattern highlights the specific and sustained upregulation of Mogat1 during tumor development. To investigate whether this translated into changes in lipid storage, we examined lipid droplet content in tumor tissues and normal breast tissue. Oil Red O staining revealed a progressive increase in lipid droplets with tumor development (Supplementary Fig. 3f, g), while they remained stable in normal mammary tissue (Supplementary Fig. 3h, i). The observation of increased Mogat1 expression and lipid droplet accumulation occurring concurrently with the previously noted decline in immune cell infiltration (Fig. 1) raises the hypothesis that Mogat1-mediated alterations in lipid metabolism might contribute to both tumor growth and the establishment of an altered immune environment.

Clinical validation in 30 paired breast cancer specimens further revealed significantly elevated Mogat1 RNA levels in tumors versus adjacent normal tissue (Fig. 2i), paralleled by heightened Mogat1 protein expression and $Ki67^+$ proliferation in tumor cells (Fig. 2j, k). Pan-cancer analysis of TCGA datasets confirmed Mogat1 upregulation across multiple malignancies (Supplementary Fig. 4a), with high expression correlating with poorer overall survival in breast cancer (BRCA, Luminal A BRCA), thymic cancer (THYM), glioma (LGG), and HPV+ head and neck squamous carcinoma (HPV-HNSC) (Supplementary Fig. 4b). Notably, Mogat1 expression was highest in triple-negative breast cancer (TNBC) compared to luminal or $HER2^+$ subtypes (Supplementary Fig. 4c), aligning with its aggressive clinical course. These findings establish Mogat1 as a potentially conserved factor associated with tumor progression and poorer prognosis in both murine models and diverse human cancers. The consistent correlation between stage-specific Mogat1 upregulation, lipid pathway enrichment, increased lipid storage in vivo, and adverse clinical outcomes strongly suggests that alterations in lipid metabolism involving Mogat1 represent an important facet of tumor adaptation, warranting functional investigation into its specific roles in driving tumor growth and influencing the immune response, which we explore in subsequent sections.

Mogat1 inhibition suppresses lipid droplet formation

Given Mogat1's localization to the endoplasmic reticulum (ER), the primary site of lipid droplet formation (Fig. 3b and Supplementary Fig. 5a), we investigated its role in lipid metabolism within cancer cells, focusing on lipid droplet accumulation and diacylglycerol (DAG) production, the precursor of triacylglycerols (TG) and phospholipids (Fig. 3a,[26,27]). To functionally assess Mogat1, we used short hairpin RNAs (shRNAs) to achieve robust knockdown in a panel of human (MDA-MB231) and mouse (MMTV-PyMT, 4T1, B16F10) cancer cell lines. This efficient Mogat1 suppression enabled systematic dissection of its lipid metabolic functions (Fig. 3c and Supplementary Fig. 5b). We first performed colony formation assays to assess Mogat1's impact on long-term tumor cell survival. Consistent with this, Mogat1 knockdown significantly suppressed colony formation across all models(Supplementary Fig. 5c), while restoring Mogat1 expression in depleted cells reversed the colony formation defects (Supplementary Fig. 5c). Our findings suggest a crucial role for Mogat1 in supporting the sustained growth and survival required for colony establishment, likely through its regulation of lipid metabolism.

We next examined the effect of Mogat1 on lipid synthesis. Mogat1 knockdown significantly reduced DAG and TG levels in all tested tumor cells (Fig. 3d, e and Supplementary Fig. 5d, e). This correlated with a substantial reduction in lipid droplet accumulation, confirmed by Oil Red O (Fig. 3f and Supplementary Fig. 5g), BODIPY 493/503 (Fig. 3g and Supplementary Fig. 5h). Perilipin 2 staining further revealed impaired lipid droplet assembly upon Mogat1 knockdown (Fig. 3h–j). Conversely, restoration of Mogat1 rescued DAG and TG levels, lipid accumulation, and lipid droplet assembly. Notably, Mogat1 inhibition did not alter expression of glycerol-3-phosphate pathway enzymes (GPAT and AGPAT, Supplementary Fig. 5f), mirroring RNA-seq findings from progressive tumor stages (Fig. 2 and Supplementary Fig. 3c, d). Together, these data establish Mogat1 as a non-redundant regulator of tumor lipid droplet biogenesis and metabolic plasticity.

Interestingly, Mogat1 knockdown did not affect fatty acid uptake or the expression of fatty acid translocase protein (Cd36, Cd68, Ld1r, Scarb1, Lrp1, and Slc27a1-4), as demonstrated by BODIPY FL C16 staining (Fig. 3m, n and Supplementary Fig. 5j) and qPCR analysis (Supplementary Fig. 5k). These findings indicate that Mogat1's primary role is in lipid synthesis rather than uptake of exogenous lipids. Collectively, these findings demonstrate that Mogat1 promotes tumor cell growth by enhancing intracellular lipid synthesis.

Mogat1 inhibition effectively suppresses tumor growth in vivo

To validate the in vivo relevance of Mogat1 in tumor progression, we established mouse allograft models using multiple cancer cell lines. Consistently, MMTV-PyMT cells with Mogat1 knockdown exhibited significantly slower tumor growth compared to controls, as evidenced by reduced tumor volume and weight (Fig. 4a–c and Supplementary Fig. 6a). This effect was replicated in 4T1 breast cancer allograft (Fig. 4d–f and Supplementary Fig. 6b) and further corroborated using B16F10 melanoma cells (Fig. 4g–i and Supplementary Fig. 6c), demonstrating the consistency of Mogat1's tumor-promoting role across different cancer types.

Our initial screening revealed a striking correlation between Mogat1 expression and enhanced lipid droplet formation in breast cancer cells (Supplementary Fig. 3f, g). To establish a causal relationship, we investigated the effects of Mogat1 inhibition in both breast and melanoma tumors. Notably, Mogat1 knockdown resulted in a dramatic reduction of lipid droplets (Fig. 4j, k and Supplementary Fig. 6d, e), coinciding with significant tumor regression (Fig. 4a–i).

https://doi.org/10.1038/s41467-025-62134-w

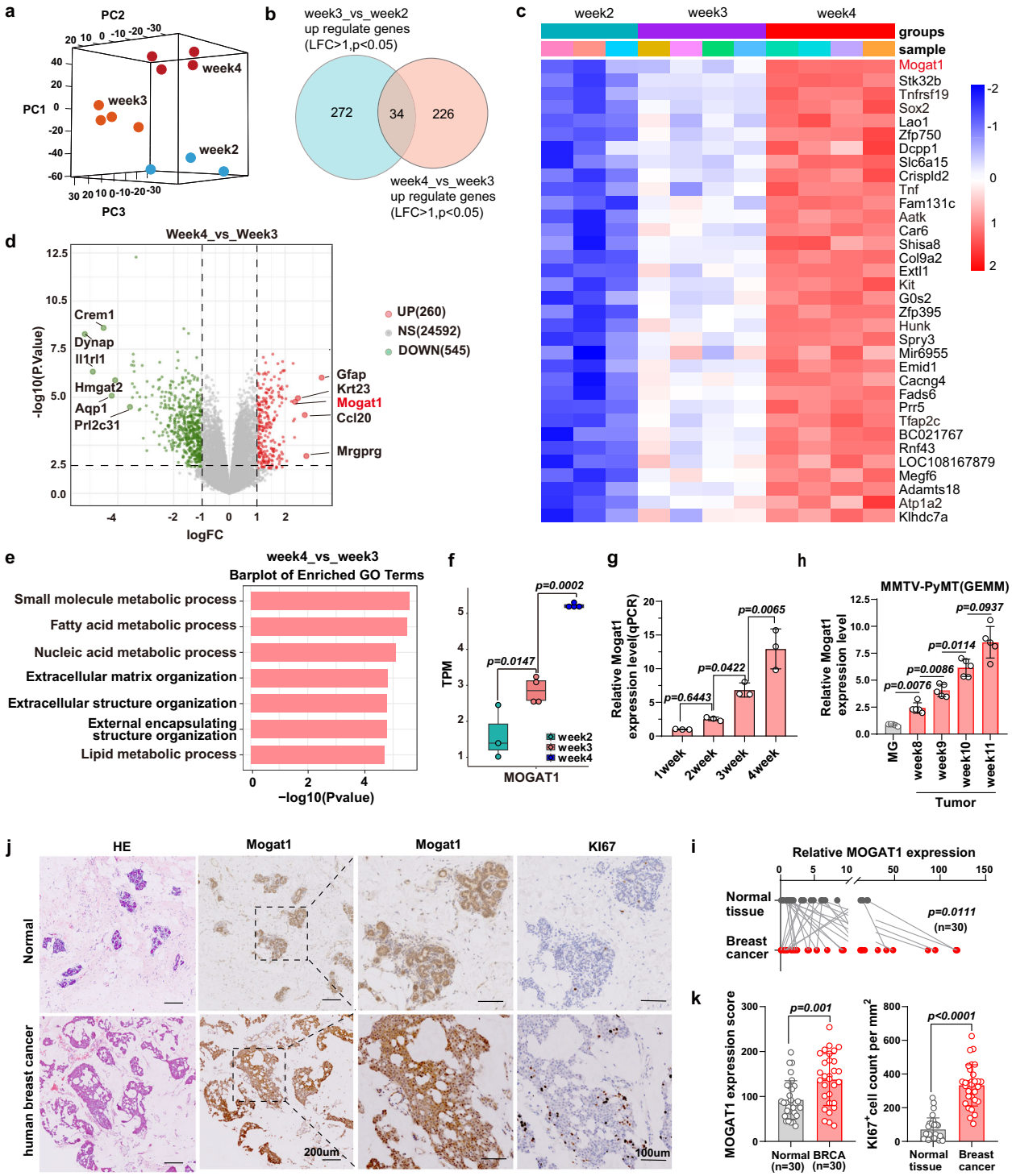

Because triglyceride synthesis and subsequent lipid droplet formation can occur via two primary pathways: the monoacylglycerol pathway and the glycerol-3-phosphate pathway[27,28]. The specific and substantial reduction in lipid droplets following Mogat1 knockdown underscores its critical and non-redundant role in this process. Notably, the inability of other enzymes in these pathways to compensate for Mogat1 depletion highlights its unique function in triglyceride synthesis and lipid droplet formation.

This in vivo tumor data not only confirms the specific role of Mogat1 in breast cancer progression but also reveals its broader implications in cancer biology. The consistent effects observed across different cancer types suggest that Mogat1-mediated lipid metabolism may represent a conserved mechanism in tumor development and maintenance. This reduction in tumor size also inversely correlated with enhanced immune cell infiltration (see more below). Collectively, these findings validate the robustness of our in vivo selection and transcriptomic profiling strategy and highlight Mogat1-driven lipid metabolism as a critical fuel source for tumor expansion.

To elucidate the molecular mechanisms underlying Mogat1's effects, we performed RNA-seq on MMTV-PyMT cells isolated from allograft (Supplementary Fig. 6f, g). Hierarchical clustering clearly distinguished Mogat1 knockdown from control tumors

Fig. 2 | Mogat1 expression increases along breast tumor advancement and correlates with lipid accumulation. a Principal component analysis (PCA) of MMTV-PyMT-GFP tumor cells sorted from tumor tissue at week 2, 3, and 4, based on variable gene expression. **b** Venn diagrams illustrating the overlap of upregulated genes in MMTV-PyMT tumors at week 3 versus week 2 and week 4 versus week 3. **c** Heatmap depicting differentially expressed genes in MMTV-PyMT tumors at week 2, 3, and 4, as determined by RNA sequencing. Each row represents a gene, and each column represents a sample. **d** Volcano plots show casing differential gene expression in MMTV-PyMT tumor cells at week 4 versus week 3. Red dots indicate upregulated genes (log2 fold change [FC] > 1, false discovery rate [FDR] < 0.05), and green dots indicate downregulated genes (log2FC < −1, FDR < 0.05). **e** Log2FC expression values of upregulated genes associated with enriched Gene Ontology (GO) terms in MMTV-PyMT tumors at week 4 versus week 3. **f** RNA-seq analysis of Mogat1 expression in MMTV-PyMT tumors at weeks 2–4 post-implantation. (n = 3 mice in week 2, n = 4 mice in week 3 and week 4). The median value (center line), lower quartile and upper quartile (box edges) and maximum and minimum value whiskers are indicated in the boxplot. **g** qPCR validation of Mogat1 expression in tumor cells sorting from MMTV-PyMT tumors at week 1–4 post-tumor induction, normalized to Gapdh and relative to week 1. (n = 3 biological tumor samples per group). **h** qPCR validation of Mogat1 expression in MMTV-PyMT GEMM tumors at week 8–11. (n = 5 biological tumor samples per group). **i** Relative Mogat1 expression by qPCR in human breast tumors and tumor-adjacent normal breast. (n = 30 breast tumors and n = 30 tumor-adjacent normal breast were analyzed. Statistics were by two-tailed paired student's t-test.). **j**, **k** Representative IHC images and quantification of Mogat1 and Ki67 expression in the indicated human breast tumor tissues and tumor-adjacent normal breast tissues. (n = 30 breast tumors and n = 30 tumor-adjacent normal breast were analyzed. Statistics were by two-tailed unpaired student's t-test.) Data are representative of two independent experiments (n = 3-4 for RNA-seq). Statistical significance was calculated using one-way ANOVA (**f**, **g**, **h**). Source data are provided as a Source Data file.

(Supplementary Fig. 6f). Differential expression analysis revealed 401 significantly upregulated and 279 downregulated genes in Mogat1-depleted tumors (LogFC > 1 or <−1, P < 0.05; Supplementary Fig. 6f). Functional enrichment analysis of upregulated genes highlighted several key processes affected by Mogat1 knockdown, including negative regulation of cell proliferation, positive regulation of programmed cell death, metabolic process regulation (Supplementary Fig. 6g). Conversely, downregulated genes were enriched in pathways related to lipid export, cell growth, calcium ion transport regulation, and cell communication (Supplementary Fig. 6g). These findings align with our in vitro observations and provide mechanistic insights into Mogat1's role in tumor progression. Collectively, these results demonstrate that Mogat1 knockdown significantly impairs tumor growth in vivo across multiple cancer models. The transcriptomic changes induced by Mogat1 depletion suggest a multifaceted role in regulating cancer cell proliferation, survival, and metabolism, underscoring its crucial role in tumor progression through changes of lipid droplet formation.

Mogat1 inhibition disrupts lipid homeostasis and energy metabolism in breast cancer

To investigate the metabolic consequences of Mogat1 inhibition in breast cancer cells, we performed non-targeted metabolomics profiling on different breast cancer subtypes GFP-labeled 4T1 tumor cells (TNBC) (Fig. 5) and MMTV-PyMT tumor cells (luminal) (Supplementary Fig. 7a) isolated from allograft tumors. Principal component analysis of the metabolomics data revealed distinct metabolic profiles between Mogat1 knockdown and control 4T1 tumor groups (Fig. 5a), with 488 metabolites downregulated and 327 metabolites upregulated upon Mogat1 knockdown (Fig. 5b, c).While multiple metabolite changes were also found in MMTV-PYMT tumors (Supplementary Fig. 7a, b).

As expected, Mogat1 inhibition led to a significant decrease in neutral lipids, particularly triglycerides and diacylglycerols (Fig. 5c). We also observed substantial changes in membrane phospholipids, including phosphatidylcholine (PC) and phosphatidylethanolamine (PE), consistent with Mogat1's role in DAG synthesis and subsequent lipid metabolism. Intriguingly, these lipid alterations were accompanied by marked changes in central carbon metabolism. Levels of glutamate, a key intermediate in glutamine metabolism and the TCA cycle, were significantly altered in Mogat1 knockdown cells, with a notable decrease in malate, suggesting impaired TCA cycle activity (Fig. 5c, d). Targeted metabolomics analysis confirmed significant downregulation of multiple TCA cycle metabolites upon Mogat1 knockdown in breast cancer (Fig. 5e–g). Further analysis revealed that Mogat1 knockdown impacted a broad spectrum of metabolic pathways, including glycerophospholipid metabolism, carbon metabolism, fatty acid metabolism, nucleotide metabolism, and sphingolipid signaling (Fig. 5h, Supplementary Fig. 7c).

These findings demonstrate that Mogat1 inhibition not only disrupts lipid droplet formation but also substantially reprograms cellular metabolism in breast cancer cells, including suppressing the TCA cycle and altering phospholipid and fatty acid metabolism. These significant alterations in intrinsic tumor cell metabolism suggest a disruption of core bioenergetic and biosynthetic pathways necessary for rapid tumor expansion. While these cell-autonomous metabolic effects likely contribute to impairing tumor fitness, their relative contribution versus the impact on the immune microenvironment in mediating the overall tumor suppression observed in vivo required further investigation, as explored in subsequent sections.

Mogat1 loss inflames tumor microenvironment

Given the critical role of the tumor microenvironment (TME) in shaping anti-tumor immunity, we next investigated the impact of tumor with Mogat1 depletion on immune cell infiltration. T-Distributed Stochastic Neighbor Embedding (tSNE) analysis of immune profiling data by FACS revealed a significant increase in immune cell infiltration into Mogat1-depleted tumors compared to controls, with a concomitant decrease in the proportion of tumor cells (Fig. 6a, d, Supplementary Fig. 8a–c).

Specifically, we observed significant increases in the infiltration of T cells, B cells, NK cells, and dendritic cells (DCs) (Fig. 6b–f). Mogat1 knockdown tumors had significantly decreased proportions of tumor-associated macrophages(TAMs), while tumor-associated neutrophils are no change (Fig. 6b, g), suggesting a shift towards a more immunogenic TME. Notably, Mogat1 knockdown led to a substantial increase in the proportion of tumor-infiltrating T cells (Fig. 6b, c, e), tumor tissue analysis using specific anti-CD8 antibody confirmed the increased abundance of intra-tumoral $CD8^+$ cytotoxic T cells in Mogat1-knockdown tumors (Fig. 6h). These suggest that Mogat1 knockdown creates a more permissive tumor microenvironment for T-cell entry, which can be crucial for mounting an effective immune response against the tumor. Interestingly, the proportion of $PD\text{-}1^+$ $CD8^+$ T cells was markedly increased (Fig. 6c, e, right). PD-1 expression on $CD8^+$ T cells typically indicates an exhausted state due to chronic antigen exposure[29–32]. In contrast, the proportion of $PD\text{-}1^+$ $CD4^+$ T cells did not change, indicating that Mogat1 inhibition specifically affects $CD8^+$ T cell activation without altering the activation state of $CD4^+$ T cells (Fig. 6e right). Intriguingly, we observed a marked increase in $PD\text{-}1^-$ $CD4^+$ and $PD\text{-}1^-$ $CD8^+$ T cells within Mogat1-knockdown tumors (Fig. 6c, e), suggesting that a portion of the T cell population remains in a non-exhausted, potentially more functional state, which could contribute to a more robust anti-tumor immune response[33–35].

To directly assess the functional state of tumor-infiltrating $CD8^+$ T cells in Mogat1-knockdown tumors, we analyzed expression of key effector and exhaustion markers. Flow cytometric analysis revealed that Mogat1 knockdown significantly increased the expression of the cytotoxic cytokines IFNγ and Granzyme B in tumor-infiltrating $CD8^+$

https://doi.org/10.1038/s41467-025-62134-w

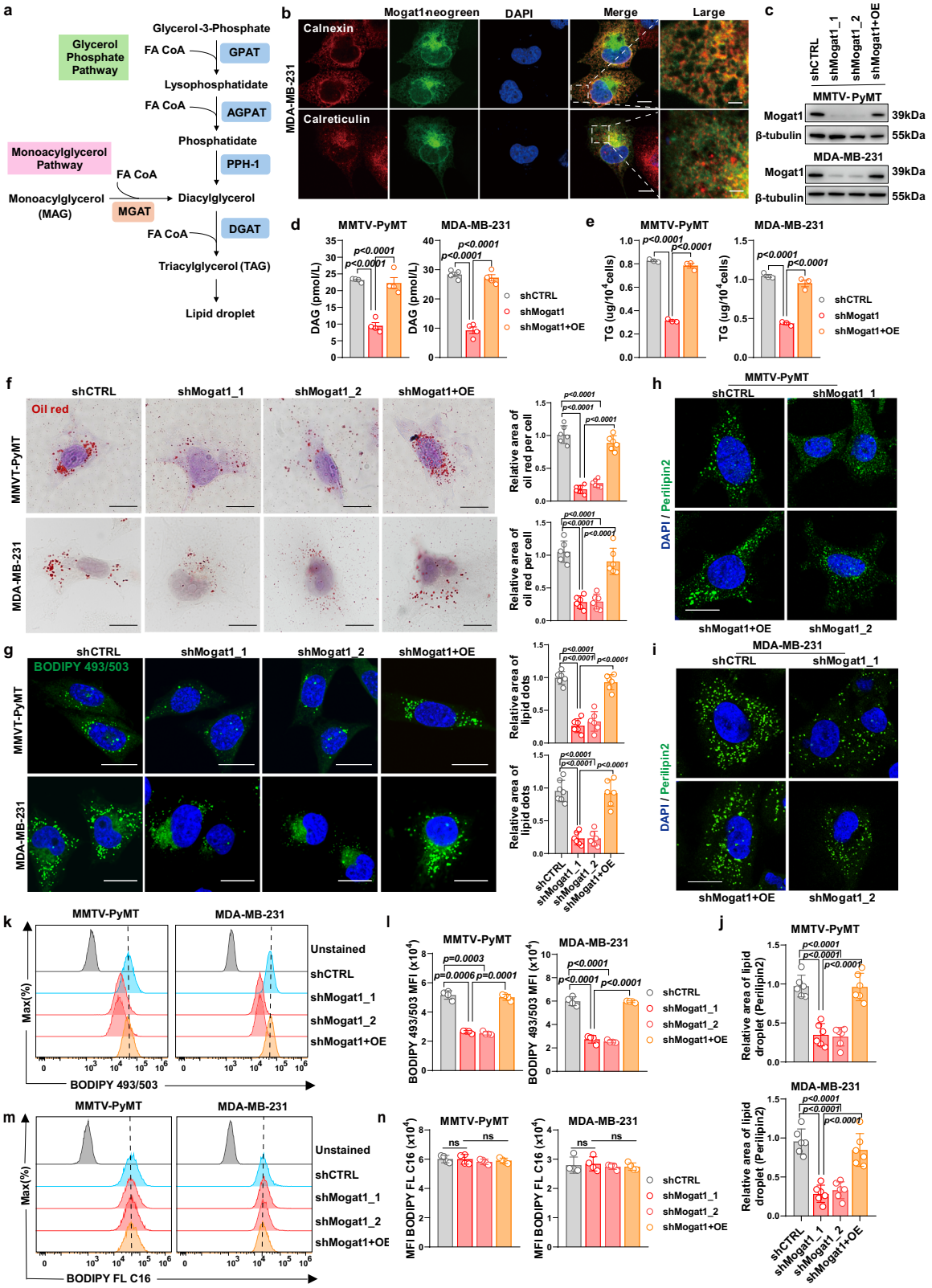

T cells (Fig. 6i). Furthermore, these cells exhibited reduced expression of the exhaustion markers TOX, CTLA-4, and LAG3 (Fig. 6j), indicating that Mogat1 depletion enhances $CD8^+$ T cell cytotoxicity while mitigating exhaustion.

Importantly, RNA sequencing of $CD8^+$ T cells isolated from Mogat1-depleted tumors revealed a distinct transcriptional profile compared to controls (Supplementary Fig. 8d). Notably, T cells from Mogat1-knockdown tumors exhibited upregulated pathways associated with proliferation, differentiation, motility, and cell adhesion, suggesting a more active and functional state[29–31]. Conversely, pathways related to T cell death, stress response, hypoxia response, and lipid metabolism were downregulated, suggesting a shift away from a dysfunctional and exhausted phenotype (Supplementary Fig. 8d). Next, we examine whether enhanced T cell infiltration translates into

Fig. 3 | Mogat1 inhibition suppresses lipid droplet formation. a Schematic of the glycerol phosphate pathway and the monoacylglycerol pathway for triacylglycerol (TAG) synthesis. Key enzymes are indicated: GPAT (glycerol-3-phosphate acyltransferase), AGPAT (1-acylglycerol-3-phosphate acyltransferase), PAP (phosphatidic acid phosphatase), DGAT (diacylglycerol acyltransferase), MGAT (monoacylglycerol acyltransferase). **b** Confocal microscopy analysis of Mogat1 localization in MDA-MB-231 cells overexpressing Mogat1 tagged with neogreen (Mogat1-neogreen). Cells were stained for endoplasmic reticulum (ER) markers Calnexin and Calreticulin. Scale bar: 10 µm. **c** Western Blot of Mogat1 knockdown efficiency and Mogat1 overexpression in MMTV-PyMT and MDA-MB231 tumor cells. Quantification of **d** diacylglycerol (DAG) and **e** triacylglycerol (TG) content in MMTV-PyMT and MDA-MB231 tumor cells. (n = 4 biological cell cultures in data **d**, n = 3 biological cell cultures in data **e**). **f** Analysis of lipid droplet content in MMTV-PyMT and MDA-MB231 tumor cells. Representative images of Oil Red O staining and quantification of Oil Red O staining intensity. Scale bar: 20 µm. (n = 6 biological cell cultures). **g** Representative confocal microscopy images of lipid droplets in MMTV-PyMT and MDA-MB231 tumor cells following Mogat1 knockdown and mogat1 overexpression. Lipid droplets are visualized with BODIPY 493/503 (green). Scale bar: 20 µm. (n = 6 biological cell cultures). **h–j** Confocal microscopy analysis of lipid droplet marker Perilipin 2 (PLIN2) in **h** MDA-MB231 and **i** MMTV-PyMT cells. **j** Quantification of lipid droplet marker Perilipin 2. Scale bar: 20 µm. (n = 6 biological cell cultures). **k**, **l** Flow cytometry analysis of BODIPY 493/503 staining (a measure of neutral lipids) in MMTV-PyMT and MDA-MB231 tumor cells. **k** Representative histograms. **l** Mean fluorescence intensity (MFI) values. (n = 4 biological cell cultures). **m**, **n** Assessment of fatty acid uptake in MMTV-PyMT and MDA-MB231 tumor cells with or without Mogat1 knockdown and mogat1 overexpression using BODIPY FL C16. **m** Representative histograms. **n** Quantification of BODIPY FL C16 uptake. (n = 4 biological cell cultures). Data in (**d**, **e**, **f**, **g**, **j**, **l**, **n**) are presented as the mean ± SD; Statistical significance was calculated using one-way ANOVA (**d**, **e**, **f**, **g**, **j**, **l**, **n**). ns, not significant. Representative immunoblots and gels shown in (**c**) were repeated at least two times independently with similar results. Source data are provided as a Source Data file.

direct increased tumor cell killing, we performed in vitro co-culture assays using primary T cells and either wild-type or Mogat1-knockdown MMTV-PyMT-OVA breast cancer and B16-OVA melanoma cells. Mogat1 knockdown did not affect tumor cell proliferation (Supplementary Fig. 8E). Importantly, Mogat1 depletion significantly increased tumor cell susceptibility to T cell-mediated lysis at all tested effector-to-target ratios (Fig. 6k, n, and Supplementary Fig. 8f, g). Crucially, control wells containing tumor cells incubated without T cells showed minimal background lysis, confirming that the observed tumor cell killing was indeed specifically mediated by the co-cultured T cells (Fig. 6k, n). This enhanced susceptibility to T cell lysis was accompanied by increased T cell cytotoxic function, as evidenced by significantly higher secretion of IFNγ and Granzyme B (Fig. 6l, m, o, p). Furthermore, chemotaxis assays demonstrated that supernatants from Mogat1-depleted tumor cells enhanced the migration and reduced cell death of activated OT1 $CD8^+$ T cells (Fig. 6q, r), suggesting that Mogat1 knockdown promotes $CD8^+$ T cell chemotaxis and infiltration into the tumor microenvironment via secreted factors. To test whether such secreted factors also modulate T cell effector function, we cultured activated $CD8^+$ T cells with conditioned media (CM) harvested from shCTRL or shMogat1 tumor cells. Indeed, $CD8^+$ T cells incubated with CM from Mogat1-depleted cells displayed significantly increased intracellular expression of both IFNγ and Granzyme B compared to those cultured with control CM (Supplementary Fig. 9a, b). This provides direct evidence that soluble factors released by Mogat1-deficient tumor cells contribute to the enhancement of $CD8^+$ T cell cytotoxic potential. Together, these in vitro findings demonstrate that Mogat1 depletion renders tumor cells more susceptible to T cell killing while simultaneously enhancing T cell effector functions, partly through the modulation of secreted factors, suggesting a multifaceted role in shaping anti-tumor immunity within the TME.

Mogat1 inhibition enhances T cell-mediated anti-tumor immunity in vivo

The enhanced T cell infiltration and intrinsic cytotoxic capacity prompted us to determine whether T cells are directly responsible for restricting tumor growth upon Mogat1 depletion in vivo. To address this, we first utilized an orthotopic MMTV-PyMT breast cancer model. T cell depletion via anti-CD4/8 antibody injection during tumor progression (Fig. 7a, b) revealed that Mogat1 knockdown-mediated tumor growth suppression was abrogated in T cell-deficient mice (Fig. 7c). Tumor growth rate, volume, and weight in Mogat1-knockdown, T cell-depleted animals were comparable to controls (Fig. 7d, e). These findings indicate that the anti-tumor immune response elicited by Mogat1 loss is primarily T cell-dependent.

Next, we verify our findings in human cancer model by employing the human breast cancer cell line MDA-MB-231 in a severely immunodeficient NOG mouse model (Fig. 7f). Consistent with previous results, Mogat1 knockdown did not significantly affect the growth rate, tumor volume, or tumor weight of MDA-MB-231 xenografts compared to controls (Fig. 7g, h). To explore the anti-tumor immune responses induced by Mogat1 knockdown, we orthotopically implanted MDA-MB-231 cells and subsequently transferred human peripheral blood mononuclear cells (PBMCs) into NOG mice deficient in both MHC class I and II molecules (Fig. 7i). By day 16, human immune cells were successfully detected in the mice's peripheral blood, prompting a second PBMC injection (Supplementary Fig. 9c). Tumor growth analysis revealed that PBMC infusion significantly suppressed tumor growth in the Mogat1 knockdown group compared to the shCTRL group, whereas Mogat1 overexpression rescued tumor growth, as demonstrated by both tumor volume and weight measurements (Fig. 7j, k). Flow cytometry indicated that intra-tumoral human immune cells were predominantly $CD8^+$ T cells (Supplementary Fig. 9d). Notably, the proportion of $CD8^+$ T cells was significantly elevated in Mogat1-knockdown tumors compared to the shCTRL group, and this increase was abrogated by Mogat1 overexpression (Fig. 7l).

Finally, to validate our findings in an alternative tumor model, we employed the B16/F10 melanoma system in Rag1-/- mice, which are deficient in T and B cells (Fig. 7m). Consistent with observations in immunocompetent mice (Fig. 4c), Mogat1 knockdown did not induce tumor shrinkage in Rag1-/- mice (Fig. 7n, o). These collective findings across multiple models, including T-cell depletion in immunocompetent mice (Fig. 7c–e), lack of efficacy in immunodeficient NOG and Rag1-/- mice (Fig. 7g, h, n, o), and PBMC-dependent suppression in a humanized system (Fig. 7j–l), demonstrate that the significant tumor suppression mediated by Mogat1 knockdown in vivo is critically dependent on T cell-mediated adaptive immunity. While Mogat1 inhibition clearly impacts intrinsic tumor cell metabolism (Figs. 3, 5), these in vivo results highlight the predominant role of extrinsic, immune-mediated effects in controlling tumor growth in an immune-competent setting. Collectively, our data show that Mogat1 depletion enhances T cell infiltration and cytotoxic capacity (Figs. 6, 7), suggesting Mogat1 inhibition operates through a mechanism involving substantial immune modulation, potentially complementing existing immunotherapies.

Synergistic enhancement of anti-tumor immunity by Mogat1 knockdown and PD-1 blockade

While essential for preventing autoimmunity by dampening excessive T cell activation, the PD-1 pathway is often exploited by tumors to evade immune destruction[36,37]. Tumor-infiltrating T cells, chronically exposed to tumor antigens, upregulate PD-1, effectively hindering their cytotoxic potential. Intriguingly, Mogat1 depletion not only led to a substantial influx of T cells into the tumor microenvironment, but also significantly increased the proportion of intratumoral $CD8^+$ T cells

https://doi.org/10.1038/s41467-025-62134-w

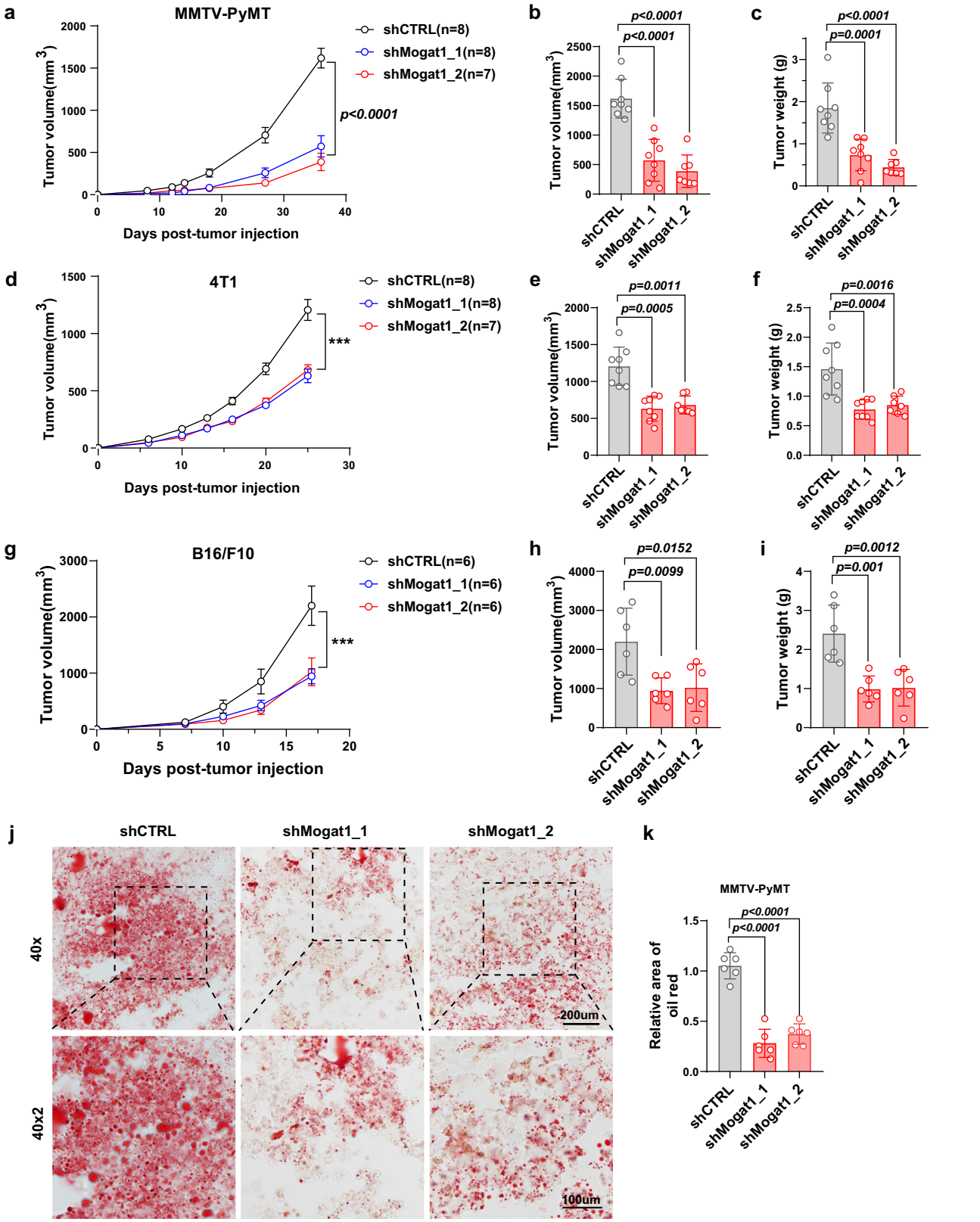

expressing PD-1. This enrichment of PD-1$^+$ CD8$^+$ T cells within the tumor, potentially rendered more susceptible to PD-1 checkpoint inhibition, prompted us to investigate whether combining Mogat1 inhibition with PD-1 blockade could synergistically enhance anti-tumor immunity.

To investigate the potential synergy between Mogat1 inhibition and PD-1 blockade, we constructed breast cancer and melanoma tumor models by injecting MMTV-PyMT or B16/F10 tumor cells, respectively. Mice were then treated with PD-1 antibodies according to a specified timeline (Fig. 8a, b). The tumor growth curves for breast cancer (Fig. 8c) demonstrated that mice injected with Mogat1 knock-down tumor cells and treated with PD-1 antibodies exhibited the slowest tumor growth. This pattern was consistently observed in the melanoma tumor model (Fig. 8d). Importantly, the combination of

Fig. 4 | Mogat1 inhibition suppresses tumor growth in vivo. a–c Growth curves of MMTV-PyMT tumors in immunocompetent FVB mice following inoculation with cells transduced with control shRNA (shCTRL, black), shMogat1_1 (blue), or shMogat1_2 (red). **b** Quantification of tumor volume and **c** weight at day 36 in the MMTV-PyMT model. (n = 8 mice in shCTRL and shMogat1_1 group, n = 7 mice in shMogat1_2 group). **d–f** Growth curves of 4T1 tumors in immunocompetent Balb/c mice following inoculation with cells transduced with shCTRL (black), shMogat1_1 (blue), or shMogat1_2 (red). **e** Quantification of tumor volume and **f** weight at day 25 in the 4T1 model. (n = 8 mice in shCTRL and shMogat1_1 group, n = 7 mice in shMogat1_2 group). **g–i** Growth curves of B16/F10 tumors in immunocompetent C57BL/6 mice following inoculation with cells transduced with shCTRL (black), shMogat1_1 (blue), or shMogat1_2 (red). **h** Quantification of tumor volume and **i** weight at day 17 in the B16/F10 model. (n = 6 mice per group). **j**, **k** Oil Red O staining of neutral lipids in tumor tissues from MMTV-PyMT mice with control shRNA (shCTRL) or two independent Mogat1 shRNAs (shMogat1_1, shMogat1_2). Scale bar: 100 μm. (n = 6 mice per group). Data are representative of two independent experiments from 6 to 8 mice per group per experiment. Data are presented as mean ± SD (**b**, **c**, **e**, **f**, **h**, **i**, **k**) and mean ± SEM (**a**, **d**, **g**). Statistical analysis was conducted by two-way ANOVA followed by Tukey's multiple comparison test (**a**, **d**, **g**). Statistical significance was calculated using one-way ANOVA (**b**, **c**, **e**, **f**, **h**, **i**, **k**). ns, not significant. Source data are provided as a Source Data file.

Mogat1 knockdown and PD-1 immunotherapy was more effective at suppressing tumor growth than either treatment alone, as confirmed by the survival curves of the mice (Fig. 8e, f). These findings collectively suggest that Mogat1 inhibition not only reshapes the TME to favor anti-tumor immunity but also enhances the efficacy of immune checkpoint blockade. Targeting Mogat1 thus holds promise as a therapeutic strategy for cancer treatment, particularly in combination with immunotherapies (Fig. 8g).

Discussion

Tumors orchestrate complex strategies to evade immune surveillance, with metabolic reprogramming emerging as a central mechanism that both supports malignant growth and shapes the immune landscape[38–41]. This metabolic adaptation is now recognized as a key driver of immune resistance, allowing tumors to manipulate the immune microenvironment to their advantage[42]. While genetic perturbation screens like CRISPR-Cas9 have transformed our understanding of gene function[4–7], these approaches may not fully capture the dynamic processes occurring during tumor progression within a complex TME[43]. Complementary strategies are needed. Here, we utilized an in vivo selection strategy coupled with transcriptomic profiling, monitoring natural gene expression changes as tumors evolve under immune pressure. This unbiased approach identified the metabolic enzyme Mogat1 as a critical mediator of immune evasion, demonstrating the power of such methods to uncover clinically relevant immune escape mechanisms operating across different stages of cancer progression[44].

While Mogat1's role in lipid metabolism is established[45,46], we reveal a function in tumor immune evasion, driven by its critical role in metabolic reprogramming during tumor progression. This metabolic reprogramming, a hallmark of cancer, is increasingly recognized as a key factor in immune evasion[47]. Our multi-stage transcriptomic analysis identified Mogat1 as central to this adaptation, with its persistent upregulation and lipid pathway enrichment suggesting tumors co-opt lipid synthesis for energy and stress resilience, consistent with the broader understanding of cancer cell metabolic flexibility[48]. We show that increased Mogat1 expression during breast cancer progression enhances lipid storage, promoting immune escape by depleting resources and inhibiting T cell infiltration, a mechanism akin to metabolic checkpoints that suppress anti-tumor immunity[49]. Critically, the anti-tumor effects of Mogat1 inhibition depend on an intact adaptive immune system, revealing a link between lipid metabolism and immune evasion, a connection also observed in other metabolic enzymes and immune pathways[50]. This discovery provides a clear mechanism for Mogat1's role in tumor progression and opens immunotherapeutic avenues, where metabolic targets are increasingly being investigated[51]. Indeed, Mogat1 inhibition suppresses tumor growth while simultaneously enhancing anti-tumor immunity, increasing T cell infiltration and augmenting their cytotoxic function, evidenced by heightened IFN-γ and Granzyme B secretion and increased tumor cell lysis. Furthermore, our findings demonstrating that secreted factors from Mogat1-depleted tumor cells enhance T cell migration and function highlight a functional interconnection between the intrinsic metabolic state and extrinsic immune modulation, mediated at least in part by soluble factors. While the precise secreted factors or cell-surface interactions downstream of Mogat1 that mediate these immune effects require further detailed investigation, representing an important avenue for future studies, our current data robustly establish the critical role of Mogat1 in regulating the tumor-immune interface.

Furthermore, our findings reveal a promising therapeutic synergy between Mogat1 inhibition and PD-1 blockade. This occurs despite a complex increase in both PD-1$^+$ and PD-1- CD8$^+$ T cells upon Mogat1 depletion. Crucially, the elevated PD-1$^+$ T cell fraction displayed heightened effector function and reduced co-expression of canonical exhaustion markers (TOX, CTLA-4, LAG3). This indicates a functionally potent, activated state amenable to PD-1 blockade[52,53], rather than terminal exhaustion. Therefore, the observed synergy likely stems from PD-1 blockade acting upon an expanded pool of these highly activated T cells fostered within the improved immune microenvironment created by Mogat1 deficiency. These results strongly support Mogat1 inhibition as a potential strategy to enhance or restore sensitivity to ICB therapies.

Methods

Experimental model and subject details

Cell culture. MDA-MB231, MMTV-PyMT, 4T1, B16/F10, MMTV-PyMT-OVA, B16/F10-OVA, and 293 T cells were devoid of mycoplasma and cultured in Dulbecco's Modified Eagle Medium (Gibco, Cat#C11995500BT), which was supplemented with 1% penicillin-streptomycin (Gibco, Cat#10378016) and 10% fetal bovine serum (Gibco, Cat#10500064). All cell lines were cultured in a humidified 5% CO_2 incubator at 37 °C and passaged at 80% confluence for a maximum of 20 passages.

Mice strains. For this research, C57BL/6 mice were supplied by the Shanghai Laboratory Animal Center, Chinese Academy of Sciences (Shanghai, China). Various female mouse strains, including FVB/N, BALB/c, NOG (NOD.Cg-Prkdc-scid Il2rgtm1sug/JicTac), and NOG-MHCI/II-2 KO (NOD.Cg-B2Mem1Tac-Prkdc-scid H2-Ab1tm1Doi Il2rgtm1sug/JicTac) aged 6–8 weeks, were procured from Beijing Vital River Laboratory Animal Technology Company (Beijing, China). The breast cancer model, female MMTV-PyMT transgenic mice (FVB/N-Tg(MMTV-PyVT)634Mul/J, JAX stock #002374), were acquired from The Jackson Laboratory (Bar Harbor, Maine, USA). All animals were housed in a specific pathogen-free (SPF) environment maintained at approximately 22 °C, provided with ad libitum access to food and water, and subjected to a 12-h light/dark cycle. Experimental procedures involving mice were performed under the ethical guidelines and regulations of China, with all protocols specifically approved by the Institutional Animal Care and Use Committee (IACUC) of Westlake University (permission numbers: 19-022-XZJ).

Human samples collection. Paired tumor and adjacent normal breast tissue samples were collected from 30 female patients undergoing surgery for breast cancer at The Affiliated Hangzhou

https://doi.org/10.1038/s41467-025-62134-w

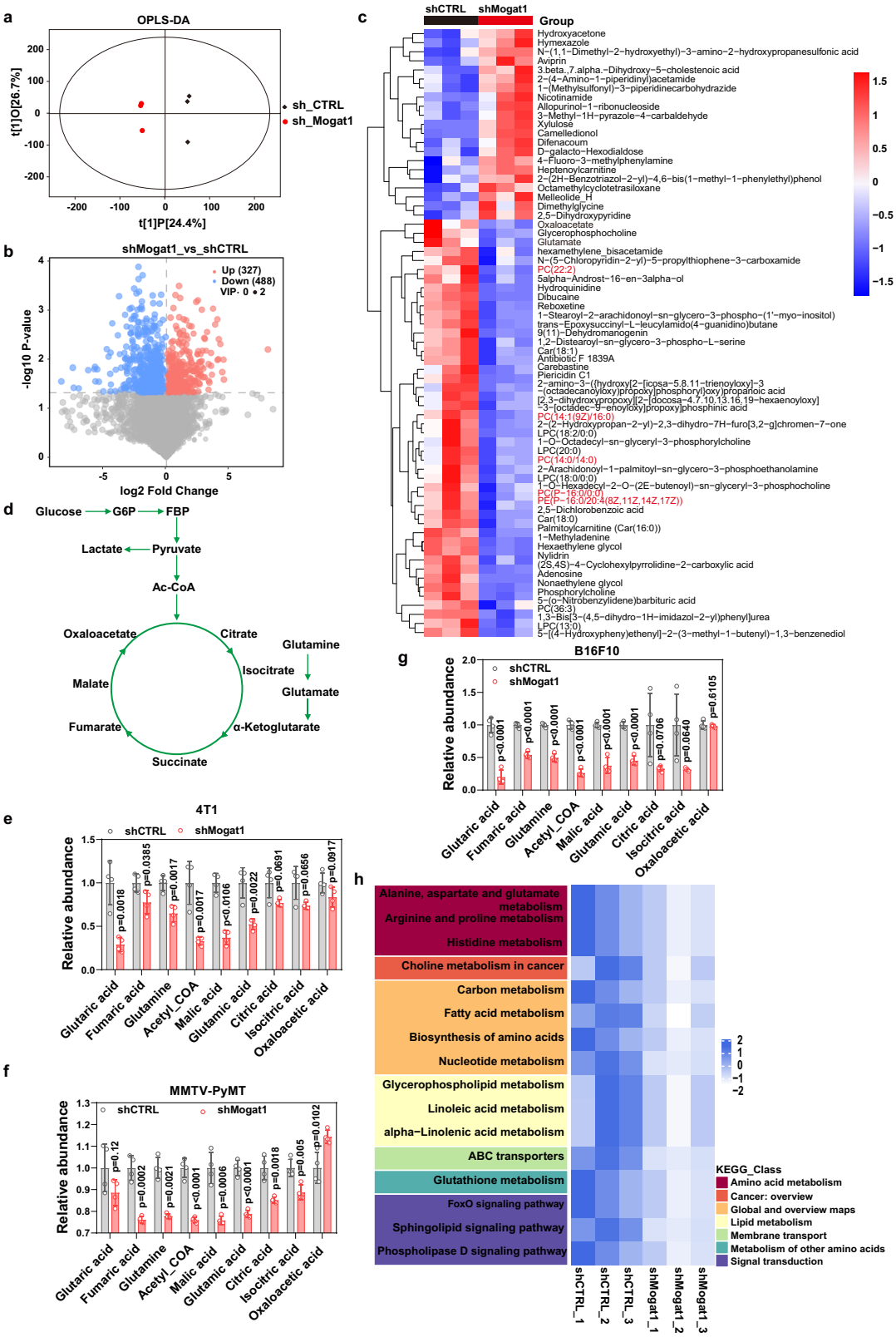

First People's Hospital. The study protocol (20240628XZJ001) was approved by the Ethics Committee of The Affiliated Hangzhou First People's Hospital, and all procedures were performed in accordance with relevant guidelines and regulations. All clinical samples were collected and analyzed with the patients' informed consent, in accordance with the approved protocol: 20240628XZJ001. In addition, all procedures involving the handling and use of human genetic resources complied with the regulations of the China Ministry of Science and Technology, and all necessary approvals were obtained. The median age of the patient cohort was 53.5 years (Interquartile Range: 47–61 years). To ensure participant de-identification, individual patient ages are presented as ranges in Supplementary Data 3. Sex/gender of participants was determined based on clinical records (assigned sex at birth). As this study focused on breast cancer in a

Fig. 5 | Mogat1 inhibition reprograms breast cancer cell metabolism by suppressing TCA cycle activity. a Orthogonal partial least squares discriminant analysis (OPLS-DA) score plot comparing the metabolic profiles of shCTRL and shMogat1 4T1 tumor cells (n = 3 biological replicates per group). **b** Volcano plot depicting differentially abundant metabolites between shCTRL and shMogat1 4T1 tumor cells. Metabolites with a variable importance in projection (VIP) score > 1 from the OPLS-DA analysis and a $P < 0.05$ from two-tailed unpaired Student's t-test are highlighted. **c** Heatmap illustrating the relative abundance of differentially expressed metabolites (VIP > 1, $P < 0.05$) identified by non-targeted mass spectrometry. **d** Schematic diagram depicting metabolic flux from glucose and glutamine into the tricarboxylic acid (TCA) cycle and glycolysis pathways. **e**–**g** Targeted mass spectrometry analysis of TCA cycle metabolites in shCTRL and shMogat1 tumor cells. **f** 4T1 cells. **g** MMTV-PyMT cells. **h** B16/F10 cells. (n = 4 biological cell cultures per group). **h** Heatmap displaying the enrichment of KEGG metabolic pathways in shCTRL and shMogat1 4T1 tumor cells, based on gene expression data. Data are representative of two independent experiments. Data in (**e**, **f**, **g**) are presented as the mean ± SD. Statistical significance was determined using a two-tailed unpaired Student's t-test. Source data are provided as a Source Data file.

cohort comprising exclusively female participants, sex/gender was not a variable in the analysis.

Method details

shRNA-mediated gene knockdown. Short-hairpin RNA (shRNA) sequences targeting Mogat1 were designed (Supplementary Data 1) and cloned into pLL3.7-GFP/PURO and inducible pTRIPZ-TurboRFP lentiviral vectors to construct shRNA plasmids. Lentivirus was produced by co-transfecting HEK293T cells with two lentiviral helper plasmids (pVSV-G and pMD8.9). The lentivirus was collected from the 48-h supernatant by passing it through a 0.45 μm filter. The collected lentivirus was either used directly to infect tumor cells with the addition of 8 μg/mL polybrene (Sigma-Aldrich, Cat#H9268) or frozen at −80 °C for later use. To eliminate negative interference, tumor cells infected with shRNA-pLL3.7-GFP/PURO lentivirus were sorted based on GFP fluorescence using a cytometry sorter (Sony MA900) or selected using puromycin. Meanwhile, tumor cells infected with shRNA-pTRIPZ-TurboRFP lentivirus were induced for RFP expression with 1 μg/mL doxycycline for 1 week and purified using a cytometry sorter (Sony MA900).

Cell colony formation assay. Tumor cells were cultured until they reached 70% confluence under optimal growth conditions. The cells were then digested into single-cell suspensions and resuspended in fresh medium. After counting, the cells were appropriately diluted and seeded into 6-well or 12-well plates at densities of 1000 or 500 cells per well, respectively. The cells were cultured in a humidified incubator with 5% CO_2 at 37 °C for 7 days, with fresh medium supplemented on day 3 without removing the old medium. Following the incubation period, cell colonies were stained with a crystal violet solution (0.5% w/v crystal violet powder, 80% v/v H2O, and 20% v/v methanol; MACKLIN, Cat#548-62-9) and imaged using a Zeiss AxioZoom V16 microscope (Zeiss, Oberkochen, Germany). Colony images were analyzed using ImageJ software.

Mouse tumor models. For the MMTV-PyMT and 4T1 orthotopic breast tumor models, 5×10^5 reconstituted tumor cells were mixed with 50% Matrigel (Corning, Cat#354234) and injected into the left fat pad of FVB and BALB/c mice, respectively. For the B16/F10 melanoma model, 2×10^5 B16/F10 cells were mixed with 50% Matrigel and subcutaneously injected into the right flank on day 0. For the MDA-MB231 orthotopic breast tumor model, 1×10^6 reconstituted tumor cells were mixed with 50% Matrigel and injected into the left fat pad of NOG mice. For human PBMC treatment, 1×10^7 human PBMC cells were injected via the tail vein into MHCI/II-DKO-NOG mice on day 0 and day 16. On day 1, 1×10^6 MDA-MB231 tumor cells were injected into the left fat pad of the mice. For anti-PD1 antibody treatments, mice were injected intraperitoneally with 200 μg of anti-PD1 antibody (BioXCell, clone RMP1-14, Cat#BE0146) on indicated days after tumor injection, with Rat IgG2a isotype antibody (BioXCell, clone 2A3, Cat#BE0089) used as a control. For T cell depletion experiment, FVB mice were injected intraperitoneally with 200 μg of anti-CD4 antibody (BioXCell, clone RMP1-14, Cat# BE0003) and on anti-CD8a antibody (BioXCell, clone RMP1-14, Cat# BE0061) indicated days after tumor injection, with Rat IgG2a isotype antibody (BioXCell, clone 2A3, Cat#BE0089) used as a control. Tumor size was measured every 3–4 days post-challenge. Measurements were taken manually by assessing the longest dimension (length) and the longest perpendicular dimension (width). Tumor volume was calculated using the formula: $V = L \times W^2/2$. Mice were euthanized via CO_2 inhalation when tumors reached 2000 mm^3 or upon ulceration/bleeding. All procedures complied with the local institutional animal ethics board (permission number: 19-022-XZJ). The maximal tumor diameter permitted by the ethics committee was no more than 2 cm for single tumor and the maximal tumor size did not exceed the limit. Humane euthanasia was performed upon reaching predefined endpoints: tumor diameter exceeding 2 cm, body weight loss >20% relative to baseline, ulceration severity >Grade 3, or observable mobility deficits.

Mouse tumor dissection and dissociation. At the conclusion of the animal experiments, tumor tissue was dissected and finely chopped into 1 mm3 pieces using a razor blade. Concurrently, a tissue digestion solution was prepared by supplementing DMEM/F12 medium (Gibco, Cat#C11330500BT) with 2 mg/mL collagenase type IV (Gibco, Cat#9001-12-1), 1 mg/mL insulin (Gibco, Cat#12-585-014), 20 U/mL DNase I (Sigma-Aldrich, Cat#9003-98-9), and 5% fetal bovine serum. The tumor tissue pieces were resuspended in the digestion solution and gently agitated for 45 min at 37 °C. Following digestion, the tumor tissue was collected via centrifugation, and residual red blood cells were removed using a blood cell lysis buffer (Beyotime Biotechnology, Cat#C3702). The digested tissue was then washed with phosphate-buffered saline (PBS) containing 2% fetal bovine serum and filtered through a 70 μm mesh to eliminate tissue clumps. Finally, single cells from the dissociated tumor tissue were counted and stored in an appropriate medium for subsequent experiments.

Staining and flow cytometry. Single-cell suspensions derived from tumors were stained with the eFluor™ 780 Fixable Viability Dye (Invitrogen, Cat#65-0865-14) at 4 °C for 20 min, followed by blocking with TruStain FcX™ PLUS (anti-mouse CD16/32 antibody, BioLegend, Cat#156604) at 4 °C for an additional 20 min. Subsequently, the cells were stained with a panel of cell surface marker antibodies, including: PE-Cy7 anti-mouse CD45 (1:200, BioLegend, Cat#S18009F), eFluor™ 450 anti-mouse CD3 (1:200, Invitrogen, Cat#48-0032-82), PerCP/Cy5.5 anti-mouse CD8a (1:200, BD Biosciences, Cat#551162), PE anti-mouse CD8a (1:200, BioLegend, Cat#100708), BV510 anti-mouse CD4 (1:200, BioLegend, Cat#100559), BUV395 anti-mouse CD19 (1:200, BD Biosciences, Cat#563557), BV605 anti-mouse CD11b (1:200, BioLegend, Cat#101257), AF700 anti-mouse Ly6G (1:200, BioLegend, Cat#127622), BV421 anti-mouse F4/80 (1:200, BioLegend, Cat#123132), BV785 anti-mouse CD279 (PD-1) (1:200, BioLegend, Cat#135225), APC anti-mouse NK1.1 (1:200, BD Biosciences, Cat#550627), PE anti-human CD45 (1:200, BioLegend, Cat#982322), FITC anti-human CD3 (1:200, BioLegend, Cat#300452), APC anti-human CD8 (1:200, BioLegend, Cat#300911), BV510 anti-human CD4 (1:200, BioLegend, Cat#300545). After surface marker staining, the intracellular proteins were stained, like BUV615 anti-mouse IFNγ (1:100, BD Biosciences, Cat#366-7311-82) and PE-eflour610 anti-mouse Granzyme B (1:100, BD Biosciences, Cat#61-8898-80). Concurrently, cells were stained for 10 min at 37 °C with BODIPY™ 493/503 and BODIPY™ FL C16. After three rounds of

https://doi.org/10.1038/s41467-025-62134-w

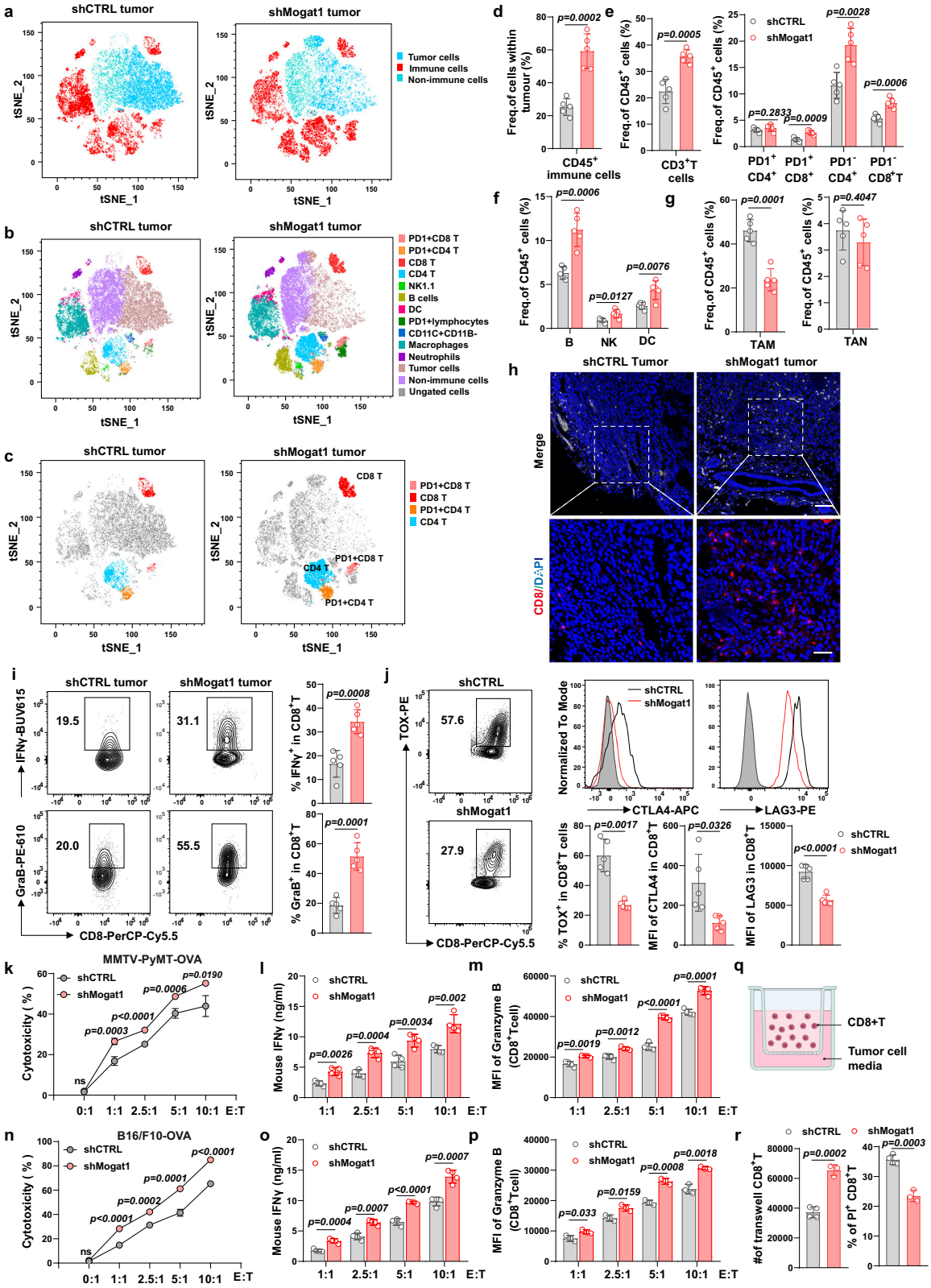

washing, the cells were analyzed using the Cytek™ Aurora (Cytek Biosciences, Fremont, CA) and CytoFLEX™ (Beckman Coulter, Fullerton, CA, USA) instruments. Data were analyzed using FlowJo™ software (v10.4.2, FlowJo LLC). Cell counts were determined by normalizing the number of cells to the recorded bead count, divided by the volume of the tumor aliquot and the mass of the tumor. The analysis gate was established based on isotype controls.

Immunofluorescence assays. For frozen tumor section, tissues were fixed in 4% paraformaldehyde (PFA) (BBI Life Sciences, Cat#E672002-0500) overnight at 4 °C and subsequently immersed in 30% sucrose overnight for infiltration. The fixed tissues were then embedded in O.C.T. compound (Tissue Tek®, Miles Scientific, Illinois) and frozen at −80 °C prior to sectioning. For cells grown on microscope slide, fixation was performed using 4% PFA at 37 °C for 15 min. After washing

Fig. 6 | Mogat1 inhibition promotes an inflamed tumor microenvironment. **a**–**c** t-distributed stochastic neighbor embedding (t-SNE) plots visualizing single-cell flow cytometry data from shCTRL and shMogat1 MMTV-PyMT tumors. **a** Total immune and non-immune cell populations. **b** All cell populations. **c** Subsets of $CD4^+$ and $CD8^+$ T cells based on PD1 expression. The comprehensive flow cytometry gating strategy for these panels is presented in Supplementary Fig. 8a, b. **d**–**g** Quantification of immune cell populations in shCTRL and shMogat1 MMTV-PyMT tumors by flow cytometry. These quantitative data (**d**) for total immune cells ($CD45^+$). **e** for total $CD3^+$T cells and T cell sub populations. **f** for B, NK and DC cells. **g** for tumor-associated macrophages (TAMs, $CD45^+CD11b^+F4/80^+$) and tumor-associated neutrophils (TANs, $CD45^+CD11b^+Ly6G^+$), were all derived using the gating strategies presented in Supplementary Fig. 8a, b. n = 5 mice per groups. **h** Representative immunofluorescence images of shCTRL and shMogat1 MMTV-PyMT tumor sections stained for CD8 (red) to visualize cytotoxic T cell infiltration. Scale bar: 100 μm. **i**, **j** FACS analysis of the IFNγ, Granzyme B (**i**) and exhaustion marker TOX, CTLA-4 and LAG3 expressing CD8 T cells infiltrating MMTV-PyMT tumors. n = 5 mice per groups. In vitro cytotoxicity assay assessing the susceptibility of shCTRL or shMogat1 (**k**) MMTV-PyMT-OVA and (**n**) B16/F10-OVA tumor cells to $CD8^+$ T cell-mediated killing. Quantification of tumor cell killing at various E:T ratios. (n = 4 biological cell cultures per group). IFNγ secretion by $CD8^+$ T cells following co-culture with shCTRL or shMogat1 **l** MMTV-PyMT-OVA and **o** B16-OVA cells, as measured by ELISA. (n = 4 biological cell cultures per group). Flow cytometry analysis of the frequency of Granzyme B-positive ($GraB^+$) $CD8^+$ T cells after co-culture with shCTRL or shMogat1 (**m**) MMTV-PyMT-OVA and (**p**) B16-OVA cells. (n = 4 biological cell cultures per group in data m, n = 3 biological cell cultures per group in data p). **q**, **r** Schematic representation of a transwell assay involving in vitro activated OT1 $CD8^+$ T cells combined with shCTRL or shMogat1 MMTV-PyMT-OVA tumor cells media. **r** $CD8^+$ T Cell migration and PI^+ dead cells were analyzed by transwell assay (n = 4 biological cell cultures in shCTRL group, n = 3 biological cell cultures in shMogat1 group). **q** is created in BioRender. https://BioRender.com/k35b440 (n = 4 biological cell cultures in shCTRL group, n = 3 biological cell cultures in shMogat1 group). Data (**a**–**j**) are representative of two independent experiments from 5 mice per group per experiment. Data (**k**–**r**) are representative of two independent experiments. Data are presented as mean ± SD. Statistical significance was calculated using unpaired Student's t tests. ns, not significant. Source data are provided as a Source Data file.

with phosphate-buffered saline (PBS), the samples were permeabilized with PBS containing 0.1% Triton X-100 (Sigma-Aldrich, Cat#V90050) for 5 min. To prevent nonspecific binding, the samples were treated with a 5% donkey serum blocking solution at room temperature for 1 h. Subsequently, the samples were incubated with primary antibodies overnight at 4 °C, including: Rat Anti-mouse CD8A (1:100, Novusbio, Cat#NBP-49045SS), Rat anti-mouse CD45(1:200, Invitrogen, Cat#14-0451-85), Goat anti-Calnexin (1:300, Abcam, Cat#ab219644), Rabbit Anti-Calreticulin (1:200, CST, Cat#12238) overnight at 4 °C. Then samples were stained with fluorophore-conjugated secondary antibodies: Donkey Anti-Rat IgG H&L conjugated 647 (Jackson Immunoreaserch, Cat#712-605-153), Donkey Anti-Rat IgG H&L conjugated 594 (Jackson Immunoreaserch, Cat#712-585-153), Donkey-anti-Rabbit AF568 (Abcam, Cat#ab175693,), Donkey-anti-Rabbit AF647 (Thermo-Invitrogen, Cat#A142730), Donkey-anti-Goat AF647 (Thermo-Invitrogen, Cat#A21447) for 1 h at room temperature. Finally, slides were stained with 1ug/mL^{1x} Hoechst (ThermoFisher, Cat#62249) for 10 min and mounted with Antifade Mounting Medium (Beyotime, Cat#P0126). Images were taken using a Olympus FV3000 Confocal (Germany) fluorescence microscope and analyzed by Image J.

In vitro T cell coculture assay. $CD8^+$ T cells were isolated from splenocytes of OVA-specific T cell receptor transgenic OT-1 mice using the EasySep™ Mouse $CD8^+$ T Cell Isolation Kit (StemCell Technologies, Cat#19853). The isolated $CD8^+$ T cells were resuspended in RPMI 1640 medium supplemented with 10% fetal bovine serum (FBS), 1% penicillin-streptomycin (P/S), 50 μM β-mercaptoethanol (Thermo Fisher Scientific, Cat#21985023), and 10 ng/mL recombinant interleukin-2 (IL-2) (PeproTech, Cat#200-02-10). The T cells were then activated with CD3/CD28 antibodies (Bio X Cell, Cat#BE0001, BE00015) for 48 h and plated at a density of 2×10^5 cells per well in a 96-well plate. Simultaneously, 1×10^4 MMTV-PyMT-OVA or B16-OVA shCTRL and shMogat1 tumor cells were seeded into a 96-well plate and allowed to adhere for 12 h. Preactivated OT-1 $CD8^+$ T cells were added to the tumor cells at various effector-to-target (E: T) ratios and co-cultured for 24 h. After co-culture, the cells were collected, and the percentage of apoptosis in tumor cells was analyzed using propidium iodide (PI) staining and flow cytometry (Beckman CytoFLEX, Fullerton, CA, USA).

$CD8^+$ T cell transwell assay. $CD8^+$ T cells were seeded into transwell inserts equipped with 5 μm transwell filters to perform a transwell migration assay. OT-1 $CD8^+$ T cells were diluted to a concentration of 1×10^6 cells/mL in T cell culture medium. A 200 μL aliquot of the T cell suspension was added to the upper chamber, while tumor cell supernatants derived from shCTRL or shMogat1 MMTV-PyMT-OVA cells cultured for 48 h were added to the lower chamber. The plates were incubated at 37 °C for 8 h. After incubation, the upper chamber was carefully removed, and cells in the lower chamber were collected, counted, and stained with propidium iodide (PI) for analysis by flow cytometry.

Determination of DAG and TAG content. Diacylglycerol (DAG) and triacylglycerol (TAG) concentrations were measured using a DAG ELISA kit (Beijing Bioroyee, Cat# RE4257) and a TAG assay kit (Beijing Solarbio, Cat# BC0625), respectively, following the manufacturer's instructions. Briefly, tumor cells were resuspended in fresh lysis buffer for DAG extraction or in triglyceride assay buffer for TAG extraction, followed by ultrasonication until the solution became clear. DAG and TAG concentrations were determined from the supernatant of each sample after generating a standard curve using a SpectraMax ABS PLUS microplate reader (Molecular Devices, Shanghai, China). The concentrations were normalized to either the total protein concentration or the tumor cell number.

Co-culture of $CD8^+$ T cells with tumor cell-conditioned media. Activated OT-1 $CD8^+$ T cells were prepared by stimulating with CD3/CD28 antibodies in complete T cell medium for 48 h. Subsequently, 1×10^6 activated T cells were seeded per well in 500 μL medium within a 12-well plate. Tumor cell-conditioned media was generated by collecting supernatants from 48 h cultures of shCTRL or shMogat1 MMTV-PyMT-OVA cells. Equal volumes (500 μL) of tumor-conditioned media were added to T cell cultures and co-incubated at 37 °C for 12 h. To facilitate intracellular cytokine detection, GolgiPlug™ Protein Transport Inhibitor (BD Biosciences, 559029) was added at 1 μL/mL 4–6 h prior to cell harvesting. Cytokine production (IFN-γ and Granzyme B) was subsequently analyzed by flow cytometry using standard intracellular staining protocols.

RNA extraction and RT-qPCR. All reagents, buffers, and containers used for RNA work were either RNase-free grade or treated with 0.1% v/v DEPC (Sigma-Aldrich, Cat# D5758) to eliminate RNase contamination in the experiments described in this section and other relevant sections. For total RNA extraction, cultured cells were washed and lysed using TRIzol reagent (Life Technologies, Cat# 15596018), following the manufacturer's instructions. Subsequently, 1 μg of RNA was reverse-transcribed into cDNA using the HiScript II Q RT SuperMix Kit (Vazyme, Cat# R223-01) according to the manufacturer's protocol. HiEff qPCR SYBR Green Master Mix (YEASEN, Cat# 11201ES) and specific primers (Supplementary Data 1) were used for real-time quantitative PCR (RT-qPCR), which was performed on a Real-time Thermal Cycler (Analytik Jena, Jena, Germany). Finally, the RT-qPCR data were normalized to GAPDH expression levels.

https://doi.org/10.1038/s41467-025-62134-w

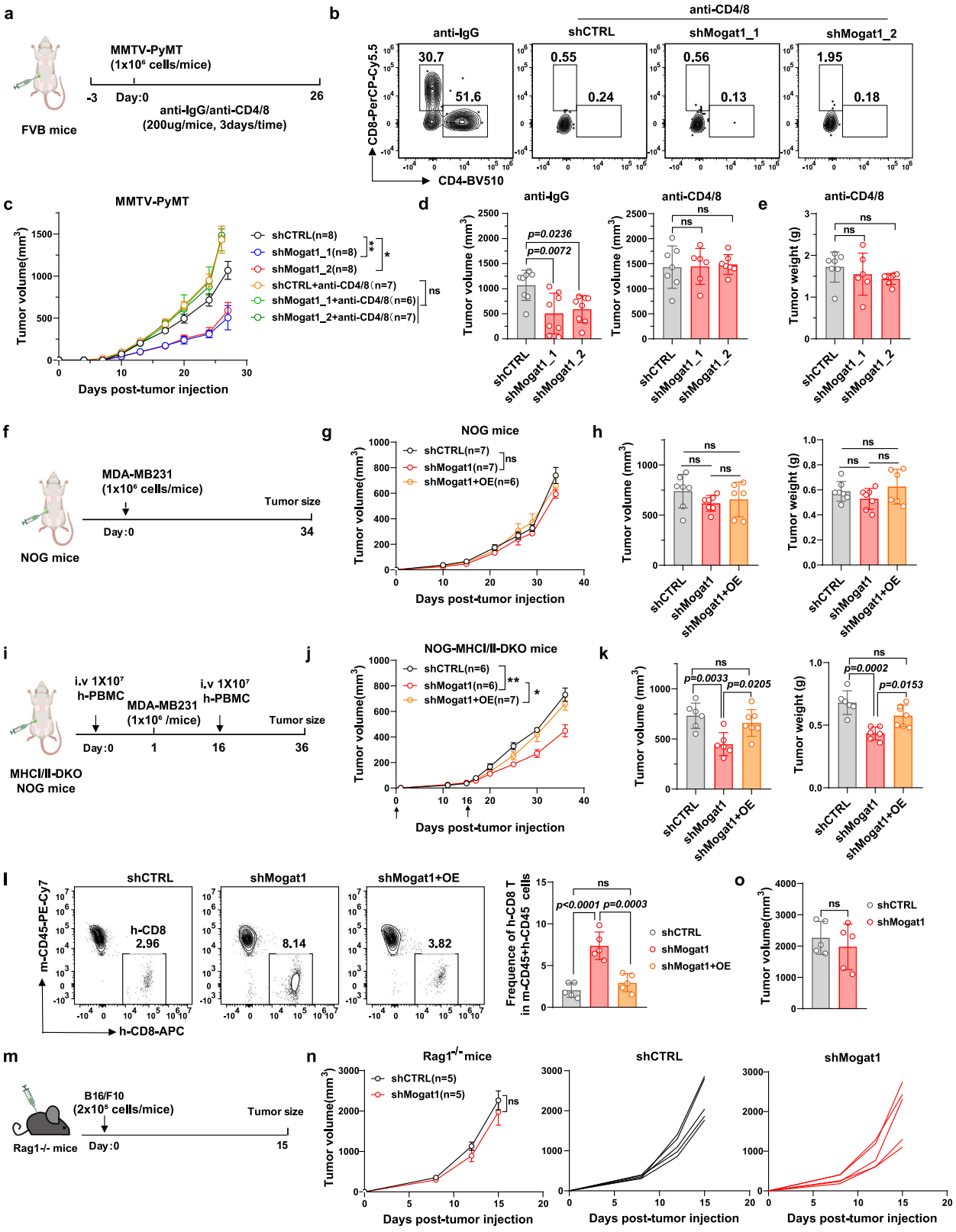

RNAseq analysis. For different cell types, cells were purified using a flow cytometry sorter (Sony MA900) based on surface markers and fluorescence, followed by total cellular RNA extraction. RNA quantification was performed using Qubit (Invitrogen, Carlsbad, USA), and RNA integrity was assessed using an Agilent Bioanalyzer (Agilent, Santa Clara, USA). Subsequently, RNA sequencing (RNA-seq) was conducted on the Illumina NovaSeq 6000 platform at Shanghai Genenergy Biomedical Technology Co., Ltd. (Shanghai, China). Raw RNA-seq data were processed using FastQC for quality control, Trim Galore for trimming, Hisat2 for mapping, and Subread for counting. Differentially expressed genes were identified using the limma software, with thresholds of log2(FC) > 1 and $P < 0.05$. Additionally, datasets of tumor cells and $CD8^+$ T cells sorted from tumor tissue have been uploaded to the Gene Expression Omnibus (GEO, accession number GSE274902).

Fig. 7 | Mogat1 loss in tumor cells stimulate anti-tumor immunity by T cells in vivo. a Schema of CD4/8 antibody depletion in orthotopic MMTV-PyMT breast tumor-bearing immunocompetent FVB mice. **b** Frequency of $CD8^+$ and $CD4^+$ T cells within tumor after inject IgG or CD4/8 antibody with flow cytometry in day 26. See Supplementary Fig. 8a, b for gating strategy. **c** Tumor growth of FVB immunocompetent mice inoculated with shCTRL and shMogat1 MMTV-PyMT tumor cells versus T cell depletion. (n = 6-8 mice per group). **d**, **e** Tumor volumes and tumor weight from (**c**) at day 26. (n = 8 mice in anti-IgG group; In anti-CD4/8 group, n = 7 mice in shCTRL and shMogat1_2 group, n = 6 mice in shMogat1_1 group). **f** Schematic representation of MDA-MB231 orthotopic tumor model in severe immunodeficient NOG mice. **g** Tumor growth of severe immunodeficient NOG mice inoculated with MDA-MB231 tumor cells. **h** Tumor volumes and tumor weight at day 34. (n = 7 mice in shCTRL and shMogat1 group, n = 6 mice in shMogat1+ OE group). **i** Schematic representation of MDA-MB231 orthotopic tumor model in MHCI/II-DKO NOG mice tail vein injected human PBMC at day 0 and day 16. (n = 6–7 mice per group). **j** Tumor growth of MHCI/II-DKO NOG mice inoculated with MDA-MB231 tumor cells. **k** Tumor volumes and tumor weight at day 36. (n = 6 mice in shCTRL and shMogat1 group, n = 7 mice in shMogat1+ OE group). **l** The proportion of tumor-infiltrating human $CD8^+$ T cells was detected by flow cytometry in MHCI/II-DKO NOG mice at day 36. Gated $mCD45^+hCD45^+$ cells. (n = 5 mice per group). The flow cytometry gating strategy is presented in Supplementary Fig. 9c, d. **m** Schema of B16/F10 melanoma animal model in $Rag1^{-/-}$ mice. (n = 5 mice per group). **n** Growth curves of B16/F10 tumors in immunodeficient $Rag1^{-/-}$ mice. **o** Quantification of tumor volume at day 15 in the B16/F10 model. (n = 5 mice per group). Data are representative of two independent experiments. Data are presented as mean ± SD (**d**, **e**, **h**, **k**, **l**, **o**) and mean ± SEM (**c**, **g**, **j**, **n**). Statistical analysis was conducted by two-way ANOVA followed by Tukey's multiple comparison test (**c**, **g**, **j**, **n**). Statistical significance was calculated using unpaired Student's t tests (**o**) and one-way ANOVA (**d**, **e**, **h**, **k**, **l**). ns, not significant. Figure (**a**, **f**, **i**, **m**) are created in BioRender. https://BioRender.com/yduci19. Source data are provided as a Source Data file.

Non-targeted mass spectrometry-based metabolomics

Sample preparation. Approximately 5×10^6 MMTV-PyMT or 4T1 tumor cells per biological replicate (n = 3 biological replicates per group: shCTRL vs. shMogat1) were collected. Cells were washed twice with ice-cold PBS. Metabolite extraction was performed by adding 1 ml of pre-chilled extraction solution (acetonitrile: methanol: water, 2:2:1, v/v/v) containing a mixture of isotopically labeled internal standards (a commercial internal standard mix was used for quality control, Shanghai Baiqu Biomedical Technology Co., Ltd., Shanghai, China). Samples were subjected to three rapid freeze-thaw cycles using liquid nitrogen and a 37 °C water bath, with vortexing for 30 s after each thaw. Protein precipitate and cell debris were removed by centrifugation at 13,000 × *g* for 15 min at 4 °C after a 10-min ice water bath. The resulting supernatant was transferred to a new tube, directly used for LC-MS analysis. Pooled quality control (QC) samples were prepared by mixing equal aliquots from each experimental sample and were injected periodically throughout the analytical run.

LC-MS analysis. Metabolomic profiling was performed using a Thermo Vanquish UHPLC system coupled to a Thermo Q Exactive HF hybrid quadrupole-Orbitrap mass spectrometer (Service Provider: Shanghai Baiqu Biomedical Technology Co., Ltd., Shanghai, China). Chromatographic separation was achieved on a Waters ACQUITY UPLC BEH Amide column (2.1 mm × 50 mm, 1.7 μm) maintained at 40 °C. The mobile phase consisted of A: [water with 25 mmol/L ammonia and 25 mM ammonium acetate] and B: [acetonitrile with 0.1% formic acid]. The LC gradient was as follows: [0-0.25 min, 95% B; 0.25-3.5 min, 95–65% B; 3.5–4 min, 65–40% B; 4–4.5 min, 40% B; 4.5–4.55 min, 40–95% B; 4.55–6 min, 95%B]. The flow rate was 0.5 mL/min, and the injection volume was 2 μL. Mass spectrometry was performed in both positive and negative ion modes using a Heated Electrospray Ionization (HESI) source. Key MS parameters were: spray voltage, 3.8 kV (positive), −3.4 kV (negative); capillary temperature, 320 °C; sheath gas flow rate, 50 Arb; auxiliary gas flow rate, 15 Arb. Full scan MS1 data were acquired over a mass range of m/z (70–1200) at a resolution of 60,000. The data were acquired in full scan and data-dependent MS/MS (ddMS2) mode.

Data processing and metabolite identification. Raw data files (.raw) were converted to (.mzXML) format using ProteoWizard msConvert (version 3.0.20287). Peak picking, retention time alignment, and feature detection were performed using XCMS package in R (V3.6.0). Metabolite annotation was performed by matching precursor m/z values (mass tolerance ± 25 ppm), retention times (tolerance ± 0.5 min), and MS/MS fragmentation patterns against an internal MS2 database (BiotreeDB, V3.0) and public database (HMDB, mona, NIST) with an MS/MS spectral match score threshold of 0.7.

Statistical analysis and pathway enrichment. The result was normalized to internal standards. Multivariate statistical analysis, including supervised Orthogonal Partial Least Squares Discriminant Analysis (OPLS-DA), was performed using SIMCA-P (16.0.2, Umetrics) to identify differentially abundant metabolites between shCTRL and shMogat1 groups. Metabolites with a Variable Importance in Projection (VIP) score >1 from the OPLS-DA model and a statistically significant difference (two-tailed Student's t-test, $P < 0.05$, with FDR correction if applied) were considered differential. Pathway enrichment analysis of these differential metabolites was performed using KEGG pathway mapping tools and R (ggplot2, V3.3.5).

The datasets have been uploaded to the China National GeneBank Database (CNGBdb, #CNP0006104, https://db.cngb.org/search/project/CNP0006104/).

Survival curve analysis using TIMER2.0. We utilized TIMER2.0, available at http://timer.comp-genomics.org/, to analyze patient survival outcomes, applying a split expression threshold of 20%. Using the "Gene_Outcome" function within the "Cancer Exploration" module of the TIMER2.0 platform, we examined the impact of the gene MOGAT1 on the survival curves of various tumors.

Statistics and reproducibility. All quantitative data from controlled laboratory experiments are presented as mean ± standard error of the mean (SEM) or mean ± standard deviation (SD), as specifically indicated in the respective figure legends. The number of biological replicates (e.g., individual mice or independent cell culture preparations) and the number of independent experimental repetitions are detailed in the corresponding figure legends for each experiment. Key experiments were independently repeated at least two to three times to ensure the reproducibility of the findings, unless otherwise specified. Sample sizes for animal experiments (typically n = 5–8 mice per group, as indicated in figure legends) were chosen based on prior experience with these in vivo models and common standards in the field, aiming to provide sufficient power to detect biologically meaningful differences while adhering to ethical animal use principles. Formal statistical power calculations were not performed prior to conducting the experiments. No data were excluded from the analyses. For animal studies, mice were assigned to experimental groups to balance for initial body age and tumor volume at the start of treatment where applicable Investigators performing tumor measurements and downstream sample processing were blinded to group allocation where practicable.

Statistical analyses were performed using GraphPad Prism (Version 8.0; GraphPad Software, La Jolla, CA, USA), Comparisons between two groups were assessed using a two-tailed unpaired Student's t-test, or a paired Student's t-test for paired samples (e.g., human tumor vs. adjacent normal tissue, as specified in figure legends). Comparisons among three or more groups were performed using one-way or two-way analysis of variance (ANOVA) followed by an appropriate post-hoc test for multiple comparisons (e.g., Tukey's, Dunnett's, or Sidak's test, as specified in figure legends). Tumor growth curves were analyzed

https://doi.org/10.1038/s41467-025-62134-w

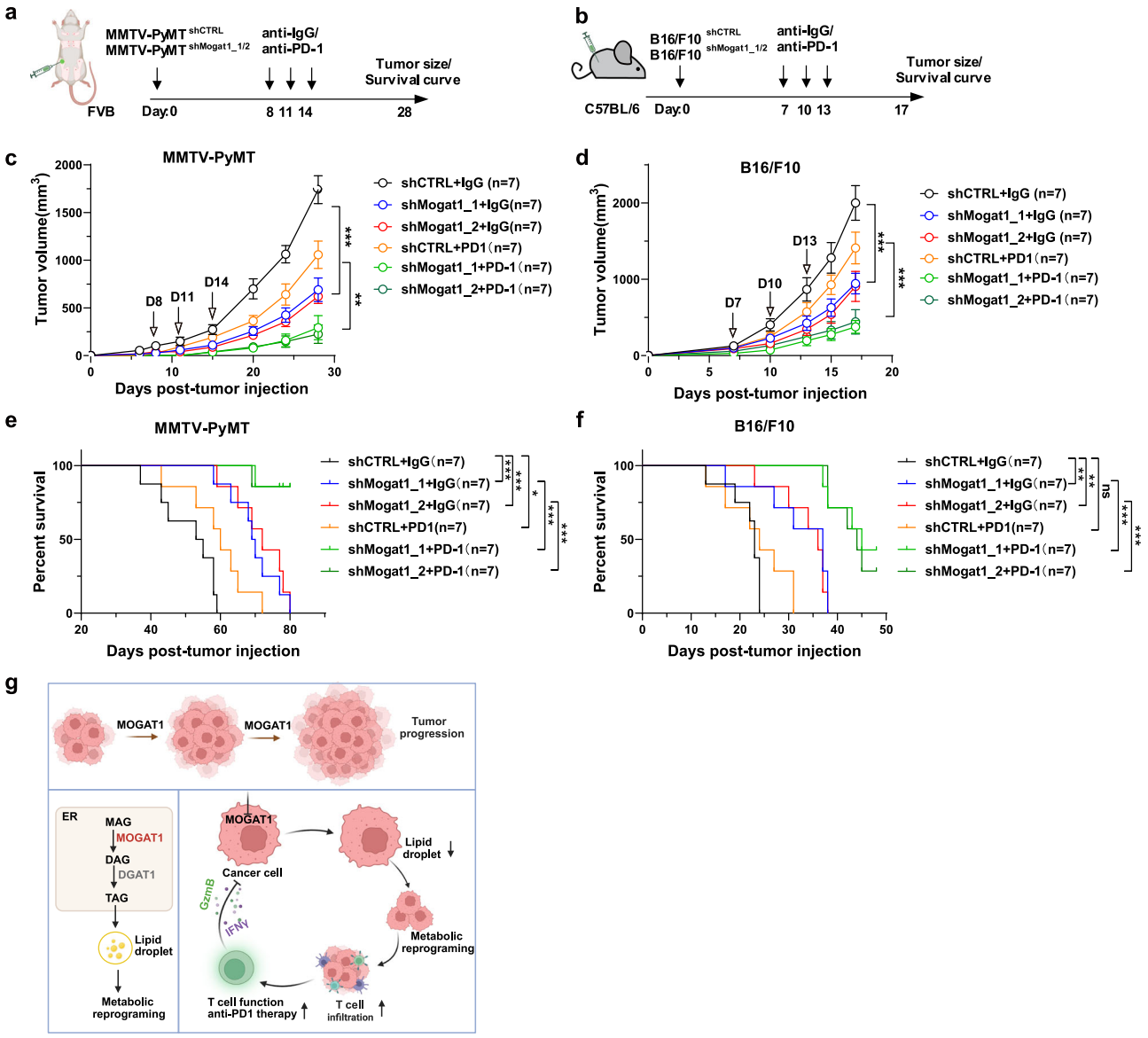

Fig. 8 | Mogat1 inhibition enhances Anti-PD-1 therapy response in breast cancer and melanoma. a, **b** Schematic representation of the experimental design for evaluating the effects of Mogat1 knockdown and anti-PD-1 therapy in mouse models. **a** MMTV-PyMT tumor cells (shCTRL or shMogat1) were implanted into FVB mice. **b** B16/F10 melanoma cells (shCTRL or shMogat1) were implanted into C57BL/6 mice. Mice received intraperitoneal injections of either IgG control antibody or anti-PD-1 antibody at the indicated time points. Created in BioRender. https://BioRender.com/9gwjt01. Tumor growth curves of **c** FVB mice in MMTV-PyMT breast cancer model and **d** C57BL/6 mice in B16/F10 melanoma model (n = 7 per group). Arrows indicate anti-PD-1 injection days. Kaplan-Meier survival curves of (**e**) FVB mice in MMTV-PyMT breast cancer model and (**f**) C57BL/6 mice in B16/F10 melanoma model (n = 7 per group). Arrows indicate anti-PD-1 injection days. **g** Graphical summary of Mogat1 drives metabolic adaptations to evade immune surveillance. Created in BioRender. https://BioRender.com/fhksjom. Data are representative of two independent experiments. Error bars in (**c**, **d**) represent standard error of the mean (SEM). Statistical significance for tumor growth curves (**c**, **d**) was determined using two-way ANOVA. Survival curves (**e**, **f**) were analyzed using the log-rank test. *P < 0.05, **P < 0.01, ***P < 0.001, ****P < 0.0001. ns, not significant. Figure (**a**, **b**, **g**) are created by BioRender. Source data are provided as a Source Data file.

using two-way ANOVA with repeated measures. Survival data were analyzed using the log-rank (Mantel-Cox) test. Correlations were assessed using Pearson's or Spearman's correlation coefficient where appropriate. Statistical significance was defined as $P < 0.05$. Specific P values are indicated in the figures or legends, with significance levels denoted as follows: *P < 0.05; **P < 0.01; ***P < 0.001; ****P < 0.0001; ns, not significant. Exact P-values are provided for key findings where appropriate.

All experiments were repeated at least two to three times, unless otherwise specified. Data are presented as mean ± Standard Error of the Mean (SEM) or Standard Deviation (SD). Graphs and additional statistical analyses were generated using GraphPad Prism Version 8. Comparisons between two groups were assessed using either unpaired or paired Student's t-tests. We employed F-test for comparing variances and two-tailed, unpaired Student's t-test to determine the statistical discrepancy for two groups. Log-rank test was used for patient survival analysis. Two-way ANOVA followed by Tukey's multiple comparison test was used for all tumor growth studies. The specific tests used, as well as the number of animals and experimental replicates, are detailed in the corresponding figure legends. Statistical significance was defined as follows: *p < 0.05; **p < 0.01; ***p < 0.001; ****p < 0.0001.

Reporting summary

Further information on research design is available in the Nature Portfolio Reporting Summary linked to this article.

Data availability

Raw and processed RNA-seq data generated in this study have been deposited to the Gene Expression Omnibus (GEO) under accession GSE274902, [https://www.ncbi.nlm.nih.gov/geo/query/acc.cgi?acc=GSE274902]. The mass spectrometry proteomics datasets have been uploaded to the China National GeneBank Database (CNGBdb, https://db.cngb.org/search/project/CNP0006104/). All the other data supporting the findings of this study are available within the article and its supplementary information files and source data. Source data are provided with this paper.

References

1. Zaretsky, J. M. et al. Mutations associated with acquired resistance to PD-1 blockade in melanoma. *N. Engl. J. Med.* **375**, 819–829 (2016).
2. Yoshihama, S. et al. NLRC5/MHC class I transactivator is a target for immune evasion in cancer. *Proc. Natl. Acad. Sci. USA* **113**, 5999–6004 (2016).
3. Sade-Feldman, M. et al. Resistance to checkpoint blockade therapy through inactivation of antigen presentation. *Nat. Commun.* **8**, 1136 (2017).
4. Gao, J. et al. Loss of IFN-γ pathway genes in tumor cells as a mechanism of resistance to anti-CTLA-4 therapy. *Cell* **167**, 397–404 (2016).
5. Manguso, R. T. et al. In vivo CRISPR screening identifies Ptpn2 as a cancer immunotherapy target. *Nature* **547**, 413–418 (2017).
6. Lawson, K. A. et al. Functional genomic landscape of cancer-intrinsic evasion of killing by T cells. *Nature* **586**, 120–126 (2020).
7. Ishizuka, J. J. et al. Loss of ADAR1 in tumours overcomes resistance to immune checkpoint blockade. *Nature* **565**, 43–48 (2019).
8. Yen, C.-L. E. et al. Identification of a gene encoding MGAT1, a monoacylglycerol acyltransferase. *Proc. Natl. Acad. Sci.* **99**, 8512–8517 (2002).
9. Liss, K. H. H. et al. Metabolic importance of adipose tissue monoacylglycerol acyltransferase 1 in mice and humans. *J. Lipid Res.* **59**, 1630–1639 (2018).
10. Agarwal, A. K. et al. Mogat1 deletion does not ameliorate hepatic steatosis in lipodystrophic (Agpat2−/−) or obese (ob/ob) mice. *J. Lipid Res* **57**, 616–630 (2016).
11. Soufi, N. et al. Inhibiting monoacylglycerol acyltransferase 1 ameliorates hepatic metabolic abnormalities but not inflammation and injury in mice. *J. Biol. Chem.* **289**, 30177–30188 (2014).
12. Gabrilovich, D. I. & Nagaraj, S. Myeloid-derived suppressor cells as regulators of the immune system. *Nat. Rev. Immunol.* **9**, 162–174 (2009).
13. Veglia, F. et al. Myeloid-derived suppressor cells in the era of increasing myeloid cell diversity. *Nat. Rev. Immunol.* **21**, 485–498 (2021).
14. Veglia, F. et al. Myeloid-derived suppressor cells coming of age. *Nat. Immunol.* **19**, 108–119 (2018).
15. Bronte, V. et al. Recommendations for myeloid-derived suppressor cell nomenclature and characterization standards. *Nat. Commun.* **7**, 12150 (2016).
16. DeNardo, D. G. & Ruffell, B. Macrophages as regulators of tumour immunity and immunotherapy. *Nat. Rev. Immunol.* **19**, 369–382 (2019).
17. Wherry, E. J. & Kurachi, M. Molecular and cellular insights into T cell exhaustion. *Nat. Rev. Immunol.* **15**, 486–499 (2015).
18. Quail, D. F. & Joyce, J. A. Microenvironmental regulation of tumor progression and metastasis. *Nat. Med.* **19**, 1423–1437 (2013).
19. de Visser, K. E. & Joyce, J. A. The evolving tumor microenvironment: from cancer initiation to metastatic outgrowth. *Cancer Cell* **41**, 374–403 (2023).
20. Singer, M. et al. A distinct gene module for dysfunction uncoupled from activation in tumor-infiltrating T cells. *Cell* **166**, 1500–1511 (2016).
21. Philip, M. et al. Chromatin states define tumour-specific T cell dysfunction and reprogramming. *Nature* **545**, 452–456 (2017).
22. Schietinger, A. et al. Tumor-Specific T Cell dysfunction is a dynamic antigen-driven differentiation program initiated early during tumorigenesis. *Immunity* **45**, 389–401 (2016).
23. Thommen, D. S. & Schumacher, T. N. T cell dysfunction in cancer. *Cancer Cell* **33**, 547–562 (2018).
24. Attalla, S. et al. Insights from transgenic mouse models of PyMT-induced breast cancer: recapitulating human breast cancer progression in vivo. *Oncogene* **40**, 475–491 (2020).
25. Lin, E. Y. et al. Progression to malignancy in the polyoma middle T oncoprotein mouse breast cancer model provides a reliable model for human diseases. *Am. J. Pathol.* **163**, 2113–2126 (2003).
26. Nye, C., Kim, J., Kalhan, S. C. & Hanson, R. W. Reassessing triglyceride synthesis in adipose tissue. *Trends Endocrinol. Metab.* **19**, 356–361 (2008).
27. Walther, T. C. & Farese, R. V. Lipid droplets and cellular lipid metabolism. *Annu. Rev. Biochem.* **81**, 687–714 (2012).
28. Olzmann, J. A. & Carvalho, P. Dynamics and functions of lipid droplets. *Nat. Rev. Mol. Cell Biol.* **20**, 137–155 (2019).
29. Blank, C. U. et al. Defining 'T cell exhaustion. *Nat. Rev. Immunol.* **19**, 665–674 (2019).
30. Ahn, E. et al. Role of PD-1 during effector CD8 T cell differentiation. *Proc. Natl. Acad. Sci. USA* **115**, 4749–4754 (2018).
31. Philip, M. & Schietinger, A. CD8+ T cell differentiation and dysfunction in cancer. *Nat. Rev. Immunol.* **22**, 209–223 (2022).
32. Behr, F. M. et al. Tissue-resident memory CD8+ T cells shape local and systemic secondary T cell responses. *Nat. Immunol.* **21**, 1070–1081 (2020).
33. van der Leun, A. M. et al. CD8+ T cell states in human cancer: insights from single-cell analysis. *Nat. Rev. Cancer* **20**, 218–232 (2020).
34. Duchemann, B. et al. CD8+PD-1+ to CD4+PD-1+ ratio (PERLS) is associated with prognosis of patients with advanced NSCLC treated with PD-(L)1 blockers. *J. Immunother. Cancer* **10**, e004012 (2022).
35. Künzli, M. et al. CD4+ T cell memory. *Nat. Immunol.* **24**, 903–914 (2023).
36. Sharpe, A. H. et al. The diverse functions of the PD1 inhibitory pathway. *Nat. Rev. Immunol.* **18**, 153–167 (2018).
37. Chamoto, K. et al. Insights from a 30-year journey: function, regulation and therapeutic modulation of PD1. *Nat. Rev. Immunol.* **23**, 682–695 (2023).
38. Martínez-Reyes, I. & Chandel, N. S. Cancer metabolism: looking forward. *Nat. Rev. Cancer* **21**, 669–680 (2021).
39. Guerra, L., Bonetti, L. & Brenner, D. Metabolic modulation of immunity: a new concept in cancer immunotherapy. *Cell Rep.* **32**, 107848 (2020).
40. Ghesquière, B., Wong, B. W., Kuchnio, A. & Carmeliet, P. Metabolism of stromal and immune cells in health and disease. *Nature* **511**, 167–176 (2014).
41. Martin-Perez, M. et al. The role of lipids in cancer progression and metastasis. *Cell Metab.* **34**, 1675–1699 (2022).
42. Hanahan, D. & Weinberg, R. A. Hallmarks of cancer: the next generation. *Cell* **144**, 646–674 (2011).
43. Sanjana, N. E. et al. Improved vectors and genome-wide libraries for CRISPR screening. *Nat. Methods* **11**, 783–784 (2014).
44. Trapnell, C. et al. Differential gene and transcript expression analysis of RNA-seq experiments with TopHat2. *Nat. Biotechnol.* **30**, 672–676 (2012).
45. Luekelittle, A. J. et al. Multiple antisense oligonucleotides targeted against monoacylglycerol acyltransferase 1 (Mogat1) improve glucose metabolism independently of Mogat1. *Mol. Metab.* **49**, 101204 (2021).
46. Singer, J. M. et al. Monoacylglycerol O-acyltransferase 1 lowers adipocyte differentiation capacity in vitro but does not affect adiposity in mice. *Obesity* **30**, 2122–2133 (2022).

47. Vander Heiden, M. G. & DeBerardinis, R. J. Understanding the intersections of metabolism and cancer biology. *Cell* **168**, 657–669 (2017).
48. Pavlova, N. N. & Thompson, C. B. The emerging hallmarks of cancer metabolism. *Cell Metab.* **23**, 27–47 (2016).
49. Pearce, E. L. & Pearce, D. A. Metabolic pathways in immune cell activation and quiescence. *Immunity* **38**, 633–643 (2013).
50. Wilfahrt, D. et al. Metabolic waypoints during T cell differentiation. *Nat. Immunol.* **25**, 206–217 (2024).
51. Agarwala, Y. et al. Targeting metabolic pathways to counter cancer immunotherapy resistance. *Trends Immunol.* **45**, 486–494 (2024).
52. Keir, M. E. et al. PD-1 and its ligands in tolerance and immunity. *Annu. Rev. Immunol.* **26**, 677–704 (2008).
53. Pauken, K. E. & Wherry, E. J. Overcoming T cell exhaustion in infection and cancer. *Trends Immunol.* **36**, 265–276 (2015).

Acknowledgements

This paper is dedicated to Dr. Zena Werb in grateful recognition of her generous guidance and unwavering support for Z.X. We thank Dr. Peter Marinkovich, Dr. Dan Yang, Dr. Xing Chang for their support. We thank Guichun Fang, Dr. Yilin Sun, and the Microcopy and EM Core Facility of Westlake University for providing support on data collection; This work was supported by Westlake University (101110066022201, 1011100660223D1, G11066021801, 101110066582301), Institutional Startup Grant from the Westlake Education Foundation (101165609901), Westlake University Research Center for Industries of the Future (210210006022215), Westlake University School of Medicine Clinical-X program, National Talents Program (101166511801), National Natural Science Foundation of China (10111006A012301), Zhejiang Provincial Natural Science Foundation of China (10116A082101) to Z.X.; We apologize for some relevant studies not being cited in the manuscript owing to space limitations.

Author contributions

Investigation: H.W., C.N., Y.S., Y.F., C.Y., J.L., Z.X. All authors contributed to data analysis. H.W. performed mammary tumors and immune cell analysis experiments and collected samples for RNA sequencing experiments. H.W., Y.S., C.Y., Y.F. performed fat-pad tumor and associated experiments. J.L. performed surgery and collected patients samples for associated analysis. C.N. performed RNA sequencing and bioinformatics analysis. Z.X. conceived and designed the experiments and wrote the manuscript with input from all co-authors.

Competing interests

The authors declare no competing interests.

Additional information

Supplementary information The online version contains supplementary material available at https://doi.org/10.1038/s41467-025-62134-w.

Correspondence and requests for materials should be addressed to Zhenjie Xu.

Peer review information *Nature Communications* thanks Rumela Chakrabarti, and the other anonymous, reviewer(s) for their contribution to the peer review of this work. A peer review file is available.

Reprints and permissions information is available at http://www.nature.com/reprints

Publisher's note Springer Nature remains neutral with regard to jurisdictional claims in published maps and institutional affiliations.

Open Access This article is licensed under a Creative Commons Attribution-NonCommercial-NoDerivatives 4.0 International License, which permits any non-commercial use, sharing, distribution and reproduction in any medium or format, as long as you give appropriate credit to the original author(s) and the source, provide a link to the Creative Commons licence, and indicate if you modified the licensed material. You do not have permission under this licence to share adapted material derived from this article or parts of it. The images or other third party material in this article are included in the article's Creative Commons licence, unless indicated otherwise in a credit line to the material. If material is not included in the article's Creative Commons licence and your intended use is not permitted by statutory regulation or exceeds the permitted use, you will need to obtain permission directly from the copyright holder. To view a copy of this licence, visit http://creativecommons.org/licenses/by-nc-nd/4.0/.

© The Author(s) 2025